

Journal Pre-proof



Comparative efficacy and mechanism of action of cardiac progenitor cells after cardiac injury

Muthukumar Gunasekaran, Rachana Mishra, Progyaparamita Saha, David Morales, Wen-Chih Cheng, Arun R. Jayaraman, Jessica R. Hoffman, Luran Davidson, Ling Chen, Aakash M. Shah, Gregory Bittle, Xuebin Fu, Antariksh Tulshyan, Mohamed Abdullah, Tami Kingsbury, Curt Civin, Peixin Yang, Michael E. Davis, Roberto Bolli, Joshua M. Hare, Sudhish Sharma, Sunjay Kaushal

PII: S2589-0042(22)00928-2

DOI: <https://doi.org/10.1016/j.isci.2022.104656>

Reference: ISCI 104656

To appear in: *ISCIENCE*

Received Date: 2 November 2021

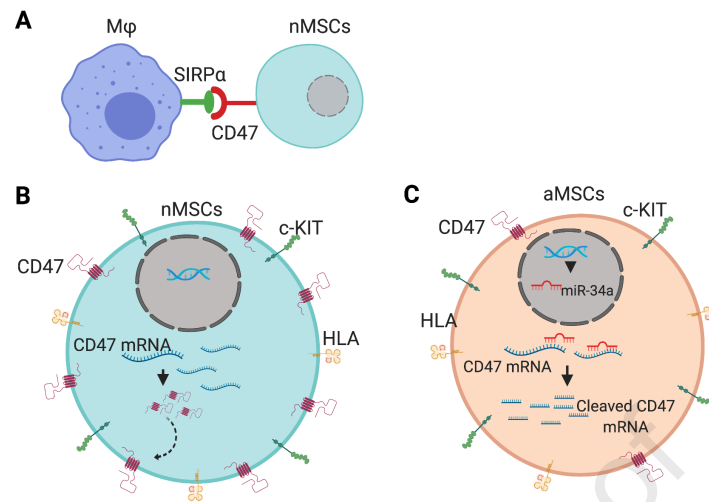
Revised Date: 8 April 2022

Accepted Date: 17 June 2022

Please cite this article as: Gunasekaran, M., Mishra, R., Saha, P., Morales, D., Cheng, W.-C., Jayaraman, A.R., Hoffman, J.R., Davidson, L., Chen, L., Shah, A.M, Bittle, G., Fu, X., Tulshyan, A., Abdullah, M., Kingsbury, T., Civin, C., Yang, P., Davis, M.E., Bolli, R., Hare, J.M, Sharma, S., Kaushal, S., Comparative efficacy and mechanism of action of cardiac progenitor cells after cardiac injury, *ISCIENCE* (2022), doi: <https://doi.org/10.1016/j.isci.2022.104656>.

This is a PDF file of an article that has undergone enhancements after acceptance, such as the addition of a cover page and metadata, and formatting for readability, but it is not yet the definitive version of record. This version will undergo additional copyediting, typesetting and review before it is published in its final form, but we are providing this version to give early visibility of the article. Please note that, during the production process, errors may be discovered which could affect the content, and all legal disclaimers that apply to the journal pertain.

© 2022



CD47 mediated phagocytosis inhibition by neonatal Mesenchymal Stem Cells: Neonatal Mesenchymal Stem Cells (nMSCs) inhibit phagocytosis in vitro and in vivo through increased CD47 expression (a,b). MicroRNA-34a regulates CD47 expression in adult MSCs (c).

In Brief: Gunasekaran et al demonstrate that human neonatal Mesenchymal Stem Cells (nMSCs) evade from macrophage mediated phagocytosis via increased CD47 expression and to promote functional recovery by secretion of exosomes and independent cytokines. The increased phagocytosis and reduced CD47 expression in aMSCs are regulated by microRNA-34a. In conclusion, our data identify a novel cell type with immune evasion, modulation and translational potential to demonstrate nMSCs as superior cell type that can be successfully translated to the clinic.

34 T 312.227.4240 | F 312.227.9643 | luriechildrens.org
35 Email: skaushal@luriechildrens.org

36
37 Sudhish Sharma, PhD
38 Departments of Surgery and Pediatrics
39 Ann & Robert H. Lurie Children's Hospital of Chicago,
40 Feinberg School of Medicine, Northwestern University,
41 225 E. Chicago Avenue, Chicago, IL 60611 USA
42 Email: susharma@luriechildrens.org
43

44

45 **ABBREVIATIONS:** aCDC, adult cardiosphere-derived cell; aMSC, adult mesenchymal stromal
46 cell; CMC, cardiomyocyte; LAD, left anterior descending coronary artery; Mφs, macrophage; MI,
47 myocardial infarction; nMSC, neonatal mesenchymal stromal cell; UCBC, umbilical cord blood
48 cell.

49

50

51

52

53

54

55

56

57

58

59

60

61

62

63

64 **SUMMARY**

65 Successful cell therapy requires cells to resist the hostile ischemic myocardium, be retained to
66 continue secreting cardioprotective growth factors/exosomes, and resist immunological host
67 responses. Clinically relevant stem/progenitor cells in a rodent model of acute myocardial
68 infarction (MI) demonstrated that neonatal cardiac mesenchymal stromal cells (nMSCs) provide
69 the most robust cardiac functional recovery. Transplanted nMSCs significantly increased the
70 number of tissue reparative macrophages and regulatory T-cells and decreased monocyte-
71 derived inflammatory macrophages and neutrophils in the host myocardium. mRNA microarray
72 and single-cell analyses combined with targeted depletion studies established CD47 in nMSCs
73 as a key molecule responsible for cell retention in the myocardium through an antiphagocytic
74 mechanism regulated by miR34a-5p. Gain and loss-of-function studies demonstrated that
75 miR34a-5p also regulated the production of exosomes and cardioprotective paracrine factors in
76 the nMSC secretome. In conclusion, miR34a-5p and CD47 plays an important role to determine
77 the composition of nMSCs' secretome and immune evasion, respectively.

78

79

80

81

82

83

84

85

86

87

88

89 INTRODUCTION

90
91 As a potential therapeutic agent, cardiac stem cells adapt to the microenvironment of the infarcted
92 myocardium and secrete specific growth factors, chemokines, cytokines, and miRNA-enriched
93 exosomes to improve cardiac function and prevent adverse cardiac remodeling after myocardial
94 infarction (MI) (Sharma et al., 2017). To optimize stem cell efficacy, it is critical to prolong stem
95 cell retention in the infarcted myocardium and to maximize the potency of the stem cell secretome,
96 which is the major mediator of stem cell function. Since the chronological age of the stem cells is
97 a major determinant of secretome potency and all clinical trials conducted so far have used stem
98 cells generated from adults (aged >18 years), clinical trials using cardiac stem cells have had
99 mixed and inconsistent results in adult patients with MI (Telukuntla et al., 2013). Additionally, a
100 recent report attributing the functional benefit of cardiac stem cell therapy to an acute,
101 inflammation-based wound-healing response that occurs even when dead cells are injected into
102 the infarcted myocardium fails to explain the positive remodeling changes in the infarcted
103 myocardium that are seen after intravenous administration of stem cells (Vagnozzi et al., 2020).
104 These results underscore the importance of more carefully examining the mechanistic basis of
105 cell therapy.

106
107 Immediately following MI, neutrophils (CD11b/c⁺/RP-1⁺) are recruited to the site of injury
108 to clear necrotic tissue and debris via their proteases. Neutrophils activate a cascade that
109 promotes macrophage polarization from proinflammatory M1 (CD68⁺/CCR2⁺) to anti-inflammatory
110 M2 (CD206⁺/CD163⁺) macrophages that secrete anti-inflammatory cytokines. Recent studies
111 have found that increased macrophage subsets or regulatory T-cells can restore cardiac function
112 and alleviate negative cardiac remodeling in injured myocardium (Frangogiannis, 2012;
113 Nahrendorf et al., 2010) (Shiraishi et al., 2016). Studies with systemic depletion of macrophages
114 or regulatory T cell (CD4⁺/FoxP3⁺/CD25⁺) subpopulations, paired with adoptive transfer of each
115 subpopulation, suggest that adaptive immunity also has an important function in regulating

116 myocardial repair (Rieckmann et al., 2019). A recent comprehensive analysis of the cardiac stem
117 cell secretome, comprising independently secreted cytokines and exosomes, has identified key
118 molecular pathways that potentially control neutrophil activation (short-lived to prevent collateral
119 damage to the myocardium), M2 polarization of macrophages, and immune rejection, which
120 together may optimize positive remodeling of the infarcted myocardium (Duran et al., 2013; Segers
121 and Lee, 2008; Vasandan et al., 2016) (Wehman and Kaushal, 2015). We investigated these
122 pathways in this study.

123
124 Thus far, in more than 200 clinical trials to treat MI, multiple stem cell types sourced from
125 various adult tissues have been evaluated with limited success. A possible reason for the
126 inconclusive results is the uncertainty regarding the mechanism of action. Accordingly, the goal
127 of this study was to elucidate the underlying mechanisms by which cardiac stem cells act to
128 restore cardiac function in the infarcted myocardium. Using single-cell RNA sequencing, and other
129 gain- and loss-of-function approaches, we investigated the efficacy of various clinically relevant
130 human stem/progenitor cells currently being tested in clinical practice. Specifically, we addressed
131 the following questions: (1) Which stem cell type most effectively repairs the injured myocardium?
132 (2) What is the effect of transplanted stem cells on immune cells? (3) How do transplanted stem
133 cells evade phagocytosis, which allows longer retention? (4) What is the overall mechanism for
134 immune evasion by the transplanted cells? (5) Can a master regulator define the composition of
135 the transplanted cell secretome? Considering the complex composition of the cellular secretome,
136 we sought to characterize the diverse phenomena targeted by transplanted cells in the host
137 myocardium and to dissect the molecular signaling pathways responsible for cardiac repair.

138

139 **RESULTS**

140 **Comparative efficacy of stem and progenitor cells in a rodent Foxn1 mutant MI model**

141 To determine the most potent progenitor cell type in a relevant, preclinical Foxn1 mutant

142 (nude) rodent MI model, we examined cardiac function after cell injection using well-studied
143 progenitor cell types in a head-to-head, blinded, randomized study. Following standard
144 characterization of each progenitor cell type (**Fig. S1a,b**), nMSCs, adult mesenchymal stromal
145 cells (aMSCs), adult cardiosphere-derived cells (aCDCs), umbilical cord blood cells (UCBCs),
146 BM-MSCs, or the placebo control containing cell-free Iscove's Modified Dulbecco Medium (IMDM)
147 were injected into the MI border zone in immunodeficient RNU rats in order to determine the
148 effects of therapy independent of the confounding influences of the immune system. Importantly,
149 all groups had similar left ventricular ejection fractions and fractional shortening at 24 hours post-
150 MI, indicating that the size of the MI was similar in all groups (**Fig. 1a, b**). Consistent with previous
151 reports, 4 weeks after the MI and injections, left ventricular function had improved significantly in
152 the groups injected with nMSCs, aMSCs, aCDCs, UCBCs, or BM-MSCs compared with placebo-
153 injected controls. More importantly, nMSCs significantly outperformed all other progenitor cell
154 types in improving the function of the injured myocardium. Histological analysis of the explanted
155 heart tissue was performed 4 weeks post-MI by Masson trichrome staining, and infarct size was
156 determined by measuring the area of fibrosis (blue) relative to the total stained myocardial area
157 (blue and pink). Regions of red staining (viable tissue) within predominately blue-stained regions
158 (fibrous tissue) were typically seen in all hearts. Examination of heart sections revealed a
159 significant decrease in fibrosis in CDCs, BM-MSCs and aMSCs treatment groups, however the
160 most significant decrease in fibrosis was identified in nMSCs treatment group (**Fig. 1c,d**).

161 To profile post-MI myocardial inflammation, histological foci of acute inflammation were
162 observed within the infarct border zone at 1-week post-MI. After 1 week, there was a significant
163 increase in activated CD68⁺ inflammatory macrophages within the areas of aMSC injection, but
164 they were significantly diminished in the areas injected with nMSCs. Staining of myocardial
165 sections also demonstrated that nMSC injection stimulated higher levels of CD163⁺ anti-
166 inflammatory macrophages (**Fig. S2a,b,c**).

167 To further evaluate the immune modulation effected by nMSCs, we performed a

168 randomized, blinded study in an immunocompetent rat model of MI in which we injected nMSCs,
169 aMSCs, or placebo (IMDM). Before injection, we assessed the angiogenic potential of selected
170 stem cell types by performing wound-healing assays on human mammary epithelial cells. The
171 wound area was significantly reduced in the presence of nMSCs compared with placebo (**Fig.**
172 **S3a,b**). Importantly, the injected nMSCs significantly outperformed aMSCs, BM-MSCs, and
173 placebo in improving ventricular function at 4 weeks in the rat MI model (**Fig. 1e,f**). We have
174 previously identified HSF1 as the a master regulator of the secretome of stem cells (Sharma et
175 al., 2017), responsible for the presence of cardioprotective factors therein. Immunoblot and RNA
176 expression analysis showed significantly higher expression of HSF1 in nMSCs as compared to
177 any other cell type showing significant improvement in cardiac function (**Fig. 1g,h, i**). Taken
178 together, our results support the idea that HSF1 represents a candidate protective mechanism
179 common to all the cell types tested, but highly expressed in nMSCs.

180

181 **Immune cell analysis following MSC injection in the Brown Norway rat MI model**

182 Immunohistochemical analysis of heart tissues after 2 days, showed significant up-
183 regulation of activated inflammatory CD68⁺CCR2⁺ or CD68⁺CX3CR1⁺ macrophage subsets in
184 hearts injected with aMSCs or the placebo control (IMDM) (**Fig. 2 a,b,d,e**). In contrast, hearts
185 injected with nMSCs showed significant decreases in these macrophage subsets (**Fig. 2 a,b,d,e**).
186 In addition, the injected nMSCs significantly increased anti-inflammatory CD68⁺CD163⁺
187 macrophage levels compared with the other study groups (**Fig.2c,f**).

188 Using single-cell suspensions from freshly-obtained, leukocyte-enriched fractions of whole
189 hearts at 5 days post-MI, we analyzed macrophages, neutrophils, T cells, T regulatory cells
190 (Tregs), and dendritic cells by flow cytometry. Compared with injection of placebo, we found that
191 the injected nMSCs significantly decreased inflammatory CD68⁺/CD45⁺ macrophage levels and
192 CD11b/c⁺/R1⁺ neutrophil levels while significantly increasing CD4⁺/CD25⁺/FoxP3⁺ Treg levels
193 (**Fig. 2g,h**). All injected groups had similar levels of total T cells (CD3⁺), cytotoxic T cells

194 (CD3⁺/CD8⁺), and dendritic cells (CD45⁺/CD11c⁺/MHC-CII) (**Fig. S4a–g**).

195 To further assess cardiac function in an immunocompetent rat MI model, we injected
196 human cardiac-derived nMSCs and their adult counterparts, aMSCs, in the infarcted myocardium
197 with and without immunosuppressive treatment involving cyclosporine A (CSA). Compared with
198 injection of aMSCs or the placebo control (IMDM), injection of nMSCs produced significant
199 improvement in cardiac function (**Fig. S5a–d**). Importantly, injection of aMSCs with CSA treatment
200 significantly improved cardiac function when compared with injection of aMSCs alone at 4 weeks
201 post-MI (**Fig. S5a,b**), suggesting that dampening the immune response is critical for optimizing
202 the cardiac reparative potential of aMSCs. Strikingly, injected nMSCs significantly improved
203 cardiac function independent of CSA treatment (**S5c,d**), suggesting active immunomodulation.
204 During the post-treatment period, injected nMSCs significantly dampened levels of the
205 inflammatory cytokines interleukin (IL)-4 and IL-12 but increased levels of anti-inflammatory IL-10
206 in plasma collected on post-injection days 2 and 7 in the same MI rat model (**Fig. S6a–c**),
207 consistent with immunomodulatory action.

208

209 **nMSCs evade phagocytosis *in vivo* and *in vitro***

210 Studies from our laboratory and others have demonstrated that injected progenitor cells
211 fail to differentiate into mature cardiomyocytes in the MI model; thus, an alternative mechanism
212 must be responsible for functional recovery (Sharma et al., 2017). Through a deep proteomic
213 analysis, we previously determined that the complete secretome, comprised of independently
214 secreted cytokines and exosomes, is the progenitor cell compartment with the ability to fully
215 functionally repair the myocardium post-MI (Sharma et al., 2017). Beyond the immune modulation
216 mechanism defined above, we additionally explored 3 potential mechanisms by which nMSCs
217 may promote functional recovery of the injured myocardium: cell retention; independently
218 secreted cytokines; and secreted exosomes. To explore these molecular pathways, we performed
219 a comparative analysis of nMSCs and aMSCs.

220
221 First, to determine if nMSCs increase cell retention by inhibiting phagocytosis, we
222 performed *in vitro* and *in vivo* phagocytosis assays with green fluorescent protein (GFP)-labeled
223 nMSCs (nMSC^{GFP+}) and aMSCs (aMSC^{GFP+}) using macrophages derived from THP-1 cells as the
224 phagocytic cells (**Fig. 3a, b,**). aMSCs^{GFP+} significantly increased phagocytosis by M1 PKH26
225 macrophages in a co-culture experiment. In contrast, nMSCs^{GFP+} inhibited phagocytosis by M1
226 PKH26 macrophages, enabling nMSCs^{GFP+} proliferation (**Fig. 3c,d,**). Similarly, injection of
227 nMSCs^{GFP+} in the immunocompetent **Brown Norway** rat MI model resulted in minimal
228 phagocytosis and thus significantly increased cell retention. In contrast, injection of aMSCs^{GFP+}
229 resulted in increased phagocytosis and minimal cell retention (**Fig. 3e,f**). These results are
230 consistent with current models of cancer cell proliferation and migration in which tumor
231 progression is promoted by an antiphagocytic mechanism that dampens the inflammatory
232 response and facilitates cancer cell immune evasion (Alvey and Discher, 2017; Métayer et al.,
233 2017).

234

235 RNA sequencing of nMSCs and aMSCs

236 To further determine the cellular mechanism underlying the antiphagocytic actions of
237 nMSCs, we performed bulk RNA sequencing (Illumina TruSeq with a minimum of 25 million
238 paired-end reads per sample) to identify mRNAs that are differentially expressed in nMSCs and
239 aMSCs. Among the top hits affecting immunomodulation, CD47 mRNA expression was 1.7-fold
240 higher in nMSCs than in aMSCs ($P = 0.015$) (**Fig. 4a-c, Table S1**). This was consistent with our
241 previous deep quantitative comparative proteomic analysis, which revealed CD47 to be among
242 the 8 most highly represented proteins in nMSCs compared with aMSCs (Sharma et al., 2017).
243 CD47 is a key antiphagocytic molecule and is up-regulated by a variety of cancers, rendering
244 malignant cells resistant to phagocytosis stimulated by the immune surveillance machinery (Chao

245 et al., 2012; Jaiswal et al., 2009; Kamerkar et al., 2017; Majeti et al., 2009; Willingham et al.,
246 2012b; Zhang et al., 2018).

247

248 To further resolve the differences between nMSCs and aMSCs, cells were sequenced
249 with 10x Genomics single-cell technology and analyzed for transcriptional heterogeneity across
250 cell subpopulations (**Fig. 4d**). nMSCs and aMSCs were clustered into 4 groups using the Leiden
251 community detection algorithm (**Fig. 4e**). Gene expression analysis indicated that the first 2
252 clusters had high expression of CD47, platelet-derived growth factor subunit A (PDGF-A),
253 hepatocyte growth factor (HGF), insulin-like growth factor 1 (IGF-1), fibroblast growth factor 2
254 (FGF-2), vascular endothelial growth factor A (VEGF-A), and stromal cell-derived factor
255 (SDF1/CXCL12) (**Fig. 4f**), with nMSCs especially overrepresented in Cluster 2, whereas aMSCs
256 were overrepresented in cluster 3 (**Fig. 4g**). Cluster 3 had especially low expression of CD47 and
257 SDF1/CXCL12 compared with the other 3 clusters. Notably, Cluster 4 makes up a significantly
258 smaller proportion of cells (3%) than the other cell clusters (Cluster 1: 39%; Cluster 2: 29%;
259 Cluster 3: 29%). Up-regulated genes in the nMSC-enriched Cluster 2 were associated with the
260 cell cycle and proliferation, whereas those in the aMSC-enriched Cluster 3 correlated with
261 leukocyte migration and cell death(**Fig. 4h-i**). Similar analyses of Clusters 1 and 4 indicate that
262 the former is up-regulated in genes associated with integrin interactions, supramolecular fiber
263 organization, and the wound-healing response, whereas the latter is up-regulated in genes
264 involved in ribosomal activity and the VEGF-A–VEGF receptor 2 signaling pathway (**Fig. S7a**). In
265 addition, fibronectin gene expression, which was previously implicated as an essential cardiac
266 repair protein in nMSC-based therapies (Konstandin et al., 2013), is up-regulated in Cluster 1
267 cells (**Fig. S7b**). These results indicate that the differing functional responses of aMSCs and
268 nMSCs may be attributed to a few subpopulations of cells. Specifically, increased phagocytosis
269 associated with aMSCs may be attributed to the relatively high abundance of Cluster 3 cells in
270 the population, whereas the increased proliferative and adhesive properties of nMSCs may be

271 attributed to the higher abundance of Cluster 1 and 2 cells.

272

273 **CD47 expression on nMSCs inhibits phagocytosis**

274 To determine if the elevated CD47 expression in nMSCs might be responsible for
275 preventing their phagocytosis, we evaluated CD47 expression in 3 biological replicates (from 3
276 patients) of nMSCs and aMSCs by immunoblot and observed significantly higher CD47
277 expression in nMSCs (**Fig. 5a,b**). Comparative RNA expression analysis also showed
278 significantly higher expression of CD47 in nMSCs as compared to any other cell type showing
279 significant improvement in cardiac function (**Fig. 5c**). To further demonstrate that CD47 mediates
280 inhibition of nMSC phagocytosis, we performed *in vitro* and *in vivo* phagocytosis assays by
281 blocking CD47 in nMSCs using a specific antibody to CD47 (α -CD47) or its isotypic control (Alvey
282 and Discher, 2017; Chao et al., 2012; Goto et al., 2014). In co-culture with M1 PKH26
283 macrophages, nMSCs $^{\alpha$ -CD47 showed significantly increased phagocytosis compared with nMSCs $^{\alpha$ -
284 isotype (**Fig. 5d, e**). Similarly, phagocytosis was significantly increased in rats injected with nMSCs $^{\alpha$ -
285 CD47 compared with nMSCs $^{\alpha$ -isotype (**Fig. 5f, g**). Compared with nMSCs $^{\alpha$ -isotype or IMDM controls,
286 injection of nMSCs $^{\alpha$ -CD47 significantly diminished cardiac functional recovery, as assessed by
287 echocardiography at 28 days (**Fig. 5h, i**). Similarly, compared with scrambled siRNA or placebo
288 IMDM treatments (**Fig. 5j,k**), treatment of nMSCs with CD47 siRNA resulted in significantly
289 decreased cardiac functional recovery. CD47 knockdown in nMSCs by siRNA was validated by
290 immunoblot (**Fig. S8**).

291

292 **MicroRNA-34a-regulates CD47 and exosome secretion in nMSCs**

293 To gain insights into regulation of CD47 and total secretome production, including
294 independently secreted cytokines and exosomes, we examined the differential expression of
295 microRNAs (miRNAs) in nMSCs and aMSCs by microarray analysis using the μ Paraflo
296 Microfluidic Biochip and human arrays 2555. Principal component analysis of the data showed:

297 a) segregation of nMSCs and aMSCs into 2 distinct groups, suggesting a direct role of aging on
298 the miRNA composition of these cells; and b) remarkable similarities among biological replicates
299 of nMSCs but profound variance among aMSCs (**Fig. 6a,b**). Among the top 15 miRNAs with
300 significantly differential expression (>2-fold), we identified high expression of 4 miRNAs in aMSCs
301 (**Fig. 6a-c**). Among these, miR-34a stood out as being highly expressed in aMSCs compared
302 with nMSCs (2.17-fold higher; $P = 7.28 \text{ E-}04$). Interestingly, target scan analysis of miR-34a
303 identified many target genes including those related to various cardioprotective paracrine factors,
304 exosome production, and CD47 (**Fig.6a-c**). This finding was verified by qRT-PCR in 6 different
305 biological replicates ($P > 0.01$) (**Fig. 6d**). In contrast, the expression levels of miR-34b and miR-
306 34c were not statistically different between nMSCs and aMSCs (**Fig. S9a,b**). Comparative RNA
307 expression analysis also showed significantly lower expression of miR34a in nMSCs as compared
308 to BM-MSC, CDC and aMSC (**Fig. 6e**).

309 As miR-34a controls many proapoptotic processes during advancing chronological aging
310 (Xu et al., 2012), we next examined the impact of miR-34a on the cellular properties of MSCs by
311 performing loss- and gain-of-function experiments. Using lentiviral transduction, miR-34a was
312 knocked down in aMSCs with the miR-34a sponge method and overexpressed in nMSCs with a
313 miR-34a-expressing vector; an empty vector (EV) was used as a transduction control in all
314 experiments. RT-PCR was used to confirm miR-34a knockdown in aMSCs and its overexpression
315 in nMSCs (**Fig. S9 c,d**). We found that miR-34a overexpression in nMSCs significantly reduced
316 their rate of cellular proliferation by increasing levels of the cell cycle inhibitors p16 and p21 and
317 decreasing expression of the stem cell markers NANOG, KLF4, and SOX2 (**Fig. 6h,k,l, Fig.S10**).
318 In contrast, knockdown of miR-34a in aMSCs significantly enhanced their rate of cellular
319 proliferation and decreased levels of p16 and p21 (**Fig. 6g,i,j**).

320 To evaluate whether miR-34a regulates CD47, we examined the effects of miR-34a
321 overexpression versus empty vehicle in nMSCs (nMSCs^{miR-34A-OE}). Immunoblot analysis revealed
322 that miR-34a overexpression significantly reduced CD47 expression compared with nMSCs

323 transfected with the empty vector (nMSCs^{EV})(**Fig. 6m**). In the MI model, injected nMSCs^{miR-34A-OE}
324 significantly reduced cardiac functional recovery at 28 days when compared with nMSCs^{EV} or
325 nMSCs (**Fig 6n-o**). Similarly, injected aMSCs^{miR-34a-kD} significantly improved cardiac function,
326 when compared with injection of aMSCs or aMSCs^{EV} at 28 days post-MI (**Fig. 6n,o**). Furthermore,
327 nMSCs^{miR-34A-OE} co-cultured with M1 PKH26 macrophages demonstrated significantly increased
328 phagocytosis compared with nMSCs^{EV} (**Fig. 6p,q**). Similarly, injection of nMSCs^{miR-34A-OE}
329 significantly increased phagocytosis in the rat MI myocardium compared with injection of
330 nMSCs^{EV} (**Fig. 6r,s**).

331

332 **MicroRNA-34a regulates secretome production in MSCs**

333 Independently secreted cytokines are key secretome components and, significantly, are
334 present at higher levels in nMSCs than in aMSCs (Sharma et al., 2017). To further delineate
335 whether miR-34a controls independently secreted cytokines in the secretome, we quantified 7
336 key cardioprotective paracrine factors in the secretomes of aMSCs and nMSCs after knockdown
337 and overexpression of miR-34a and transfection of the empty vehicle control. ELISA-based
338 quantitative analysis of total conditioned media demonstrated that miR-34a knockdown resulted
339 in significant increases in HGF, SCF, IGF, platelet-derived growth factor beta (PDGF- β), and
340 FGF2 in the aMSC secretome (**Fig. 7a**), but did not affect levels of VEGF-A and SDF1 α . In
341 contrast, overexpression of miR-34a in nMSCs significantly decreased the levels of all 7 secreted
342 paracrine factors (**Fig. 7b**). Using computational analysis (TargetScan and Dianna Tools) to better
343 understand these effects, we determined that the mRNA transcripts of PDGF, HGF, IGF-1, FGF2
344 and SCF have direct binding sites for miR-34a in their 3' untranslated regions (UTRs)(**Fig. S11**).
345 miRNAs inhibit protein translation by binding directly to short sequence fragments in 3' UTRs. To
346 test whether miR-34a can directly target the mRNAs of these cardioprotective genes to mediate
347 the observed decreases in expression, regions of the corresponding 3'UTRs were cloned
348 downstream of firefly luciferase. In the presence of wild-type 3'UTR sequences, a significant

349 reduction in luciferase activity was seen for the PDGF, HGF, IGF-1, FGF2, and SCF genes upon
350 cotransfection with a miR-34a mimic (**Fig.7c**). Mutation of the miR-34a binding sites within the
351 3'UTR constructs blocked inhibition of luciferase expression by the miR-34a mimics,
352 demonstrating that PDGF, HGF, IGF-1, FGF2, and SCF are miR34a targets (**Fig. 7c**). As
353 promotion of angiogenesis is one of the primary mechanisms of cardiac repair by these 7
354 cardioprotective cytokines, we performed endothelial tube formation assays to determine if miR-
355 34a-related changes in protein expression regulate this functional outcome. Knockdown of miR-
356 34a in aMSCs (aMSCs^{34aKD}) resulted in a significant increase in total endothelial tube length
357 compared with vehicle alone and overexpression of miR34a in nMSCs (nMSCs^{34aOE}) (**Fig. 7d-f**).
358 Similarly, in the MI model, injected nMSCs^{miR-34A-OE} significantly reduced cardiac functional
359 recovery (**Fig. 7n,o**) and decreased formation of arterioles and neovessels as well as myocardial
360 fibrosis at 28 days when compared with nMSCs^{EV} or nMSCs (**Fig. 7j-l,o,p**). Injected aMSCs^{miR-}
361 ^{34a-KD} significantly improved cardiac function (**Fig.7n,o**), augmented the preservation/formation of
362 arterioles and neovessels, and resulted in smaller infarcted areas and reduced fibrosis when
363 compared with injection of aMSCs or aMSCs^{EV} at 28 days post-MI (**Fig. 7g-i,m.n**).

364

365 We previously showed that HSF1 not only activates key upstream regulators of cytokine
366 production to modify secretome protein enrichment of nMSCs, but also increases production of
367 exosomes in nMSCs compared with aMSCs (Sharma et al., 2017). However, the mechanism for
368 these changes in the nMSC secretome was unknown. We hypothesized that miR-34a plays a key
369 role in modifying exosome production by down-regulating the expression of HSF1 and associated
370 downstream cytokines as well as exosome levels. Indeed, we found increased levels of exosomes
371 in aMSCs^{34aKD} and reduced exosome levels in nMSCs^{34aOE}, as visualized by Nanosight (**Fig. 7q-**
372 **s, Video 1-4**), and significant enrichment of HSF1 and HSP70 expression in nMSCs compared
373 with aMSCs by immunoblot analysis (**Fig. 7t**). To further analyze the miR-34a/HSF1 axis, we
374 assessed aMSCs^{34aKD} and nMSCs^{34aOE} and showed HSP70 and HSF1 protein expression to be

375 significantly higher after miR-34a knockdown in aMSCs and significantly lower after miR-34a
376 overexpression in nMSCs (**Fig. 7u,v**). To elucidate the mechanism by which miR-34a and HSF1
377 influence exosome production, miR-34a was overexpressed in aMSCs, and quantitative RT-PCR
378 was performed for genes known to play a role in exosome biogenesis. We found that miR-34a
379 overexpression in aMSCs failed to up-regulate 3 candidate exosome biogenesis molecules:
380 VSP37a, VSP25, and CHM7 (**Fig. S12**). These proteins were up-regulated by HSF1
381 overexpression in aMSCs, (**Fig. 7w-z**). These results suggest that HSF1 (rather than miR-34a)
382 regulates exosome biogenesis directly.

383

384 **DISCUSSION**

385 Many aspects of successful cardiac repair by transplanted cardiac stem cells can be
386 greatly influenced by variables that depend on both the host response and the characteristics of
387 the transplanted cells, including stem cell retention, secretome composition, and immunorejection
388 (Sharma et al., 2017). Until now, transplanted cardiac stem cells and the host response to cellular
389 therapy have been considered separately, as many studies have used immunocompromised or
390 immunosuppressed animal models. A clinically relevant model must acknowledge that the
391 ischemic myocardium during cellular therapy is a composite of the host, the transplanted cells,
392 and their interactions. Herein, we took an integrated approach to identify the most effective
393 cardiac cell type for repairing the ischemic myocardium in the setting of an immunocompetent
394 host response to address the crucial question of how the secretome of the transplanted cardiac
395 stem cells interacts with the immune cells present in the ischemic myocardium.

396

397 We evaluated the therapeutic potential of 5 clinically relevant cell types in
398 immunocompromised animals (RNU rats) with MI. Nude rats were first used to assess therapeutic
399 potential in isolation, because normal immunocompetent animals have varying levels of tolerance
400 for different transplanted cell types. In a head-to-head comparison, we demonstrated that nMSCs

401 outperformed all other clinically tested cell types in improving cardiac function in the rat MI model.
402 We next provided several lines of evidence that, from a translational point of view in an
403 immunocompetent MI rodent model, cardiac repair is optimized by robust cellular retention, which
404 in turn directly modulates the host immune response through the secretome of the transplanted
405 cells to restore cardiac function and alleviate left ventricular remodeling. The reductions in
406 neutrophils and monocyte-derived circulating macrophages and the increases in Tregs and M2
407 macrophages in the ischemic myocardium indicates that transplanted nMSCs do not act in a linear
408 pattern, but rather target multiple arms of the immune system. Additionally, modulation of Tregs
409 in the host myocardium established that the functional benefit of nMSC therapy is not due to an
410 acute, inflammation-based, wound-healing response that rejuvenates the infarcted area of the
411 heart (Vagnozzi et al., 2020).

412
413 Strikingly, using single-cell sequencing, we found that cell-defined characteristics
414 determined by chronological aging may affect the efficacy of cellular therapy. nMSCs provided
415 the greatest therapeutic benefit when compared with adult-derived cells. This provided the
416 opportunity to perform a direct comparison between these 2 cell types isolated with similar
417 methodology. It has been well demonstrated that cardiac repair following ischemic injury is
418 supported, at least in part, by immunomodulation and macrophage polarization (Dai et al., 2020;
419 Galuppo et al., 2017; Shiraishi et al., 2016). In an immunocompetent model, we found that the
420 superior functionality of nMSCs is due to their retention in the host myocardium and
421 immunomodulation of neutrophils, macrophages, and T cells.

422
423 To mechanistically define nMSC retention in ischemic myocardium, we took a
424 multipronged approach. First, we performed comparative deep RNA sequencing analysis of
425 nMSCs and aMSCs and identified differentially-expressed mRNAs by single-cell mRNA
426 sequencing using the 10 × Genomics platform. Differentially higher expression of CD47 in nMSCs

427 and its enrichment in all 4 clusters belonging to nMSCs made it an attractive candidate for further
428 analysis. CD47 is a transmembrane protein expressed on the surface of various solid,
429 hematologic cancers and cancer stem cells. CD47 interacts with its ligand SIRP α on
430 macrophages, resulting in inhibition of phagocytosis (16-29). The presence of CD47 on
431 cardiomyocytes prevents their phagocytosis and the clearance of dead myocytes in the ischemic
432 myocardium (Zhang et al., 2017). Herein, we highlight another antiphagocytic role of CD47 in
433 cardiac repair, resulting in prolonged retention of transplanted nMSCs. Higher CD47 expression
434 by nMSCs triggers a “don’t eat me” signal. These data are particularly provocative as other
435 stem/progenitor cells (e.g., induced pluripotent stem cells), need to express CD47 in order to
436 create an immunosuppressive response (Deuse et al., 2019). The downstream antiphagocytic
437 mechanism of CD47 action has been well-defined (Chao et al., 2012; Majeti et al., 2009;
438 Willingham et al., 2012a; Zhang et al., 2018). By computational analysis followed by experimental
439 verification, we identified miR34a-5p, an age-related microRNA, as the master regulator of CD47.

440

441 We previously demonstrated that nMSCs have greater proliferative potential than adult
442 MSCs. Additionally, compared with the aMSC secretome, the nMSC secretome contained more
443 cardioprotective paracrine factors and exosomes, explaining their greater regenerative potential
444 (Sharma et al., 2017). In our study, miR34a overexpression in nMSCs reduced both their
445 proliferative potential and cardiac recovery after MI. In contrast, miR-34a knockdown in aMSCs
446 increased their proliferative potential and significantly improved cardiac function with reduced
447 fibrosis. These results establish the critical role of miR34a in determining the quality of secretome
448 in particular and the functional activity of cell therapy as such.

449

450 We found that miR-34a overexpression resulted in decreased secretion of PDGF, HGF,
451 IGF-1, FGF2, and SCF from nMSCs. In general, miRNAs regulate the transcription of target
452 coding RNAs by binding to their 3'UTRs, inhibiting further translation and destabilizing the

453 translational complex (Seo et al., 2017). We identified and verified the presence of direct miR-34a
454 binding sites in the 3'UTR regions of the mRNAs encoding these paracrine factors, revealing
455 another level at which the functional abilities of nMSCs can be controlled. We further found that
456 overall exosome production varied inversely with miR-34a. We demonstrated previously that heat
457 shock factor 1 (HSF1) regulated both protein secretion and exosome production (Sharma et al.,
458 2017). Interestingly, overexpression of miR-34a resulted in decreased HSF1/HSP 70 expression,
459 whereas knockdown of miR-34a led to increased HSF1/HSP70 expression. Thus, miR-34a likely
460 potentiates exosome production by decreasing the expression of HSF1/HSP70 and other
461 components of this pathway. These results indicate that a miR34a-HSF1-CD47 axis is critical for
462 the ability of nMSCs to robustly improve cardiac function in the injured myocardium.

463
464 We found that nMSCs have an innate cardioprotective phenotype due to their optimal
465 secretome production, which is tightly regulated by miR-34a for both independently secreted
466 cytokines and exosomes. These results broaden our understanding of how cell therapy leads to
467 cardiac repair. In addition, our results suggest that full, effective repair of the injured myocardium
468 and the associated reversal of left ventricular dysfunction requires both cellular and biochemical
469 characteristics such as CD47 expression and secretome composition. We demonstrated that
470 miR-34a is key molecule directly affecting cellular retention by targeting CD47 and
471 cardioprotective cytokines. miR-34a, through HSF1, also affects exosome production. These
472 results establish a direct correlation between a microRNA and secretome composition affecting
473 the functional potential of a cell therapy. Interestingly, miR34a knockdown reversed the deficits of
474 aged aMSCs to recover the functional activity of the ischemic myocardium. Thus, our study shows
475 that cellular characteristics determined by chronological age have an adverse effect on the
476 efficacy of cellular therapy and that the secretome is the functional unit of nMSCs.

477

478 Limitations of study

479 A limitation of our study is that the *in vitro* conditions were different for each cell type due to their
480 source of isolation and its diversity (Hare et al., 2012; Saha et al., 2019; Sharma et al., 2017).
481 Unfortunately, it is not possible to culture and expand all the different cell populations under
482 identical conditions. Although our study demonstrated that a single cell type (nMSCs) produced
483 superior cardiac functional recovery compared to other cells types, a combinatorial approach
484 using different cell types together might provide superior benefits to any one cell type by promoting
485 multiple concurrent processes such as modulation of immunity, influencing remodeling, and
486 favoring angiogenesis or other beneficial tissue responses (Lim et al., 2014). Transgenic
487 knockouts of specific subpopulations of macrophages will be necessary to delineate their precise
488 role(s) in cardiac functional recovery after nMSC injection in rats with MI (Vagnozzi et al., 2020).
489 As such rat models are not currently available, we cannot definitively identify the macrophage
490 population that mediates the beneficial effects of nMSCs. However, our study demonstrates that
491 nMSC transplantation induces significantly higher levels of CD163⁺ anti-inflammatory
492 macrophages and reduces inflammatory CD68⁺CCR2⁺ and CD68⁺CX3CR1⁺ macrophages,
493 confirming that nMSCs actively modulate the inflammatory response in the rat MI model. Our
494 results confirm that CD47 expression in nMSCs helps these cells to evade phagocytic
495 macrophages, thereby enhancing cardiac functional recovery after MI. However, other factors
496 such as resistance to environmental stress, anti-apoptosis, increased cell adhesion molecules
497 expression, and genes associated with cell cycle and proliferation may contribute to increased
498 cell survival and retention in the infarcted myocardium *in vivo*.

499

500 CONCLUSIONS

501 Our data identify nMSCs as a potent cell type with translational potential and illuminate
502 cellular mechanisms responsible for the beneficial effects of stem cell therapy. Together, our data

503 strongly support the concept that nMSCs promote functional recovery of the heart via an active,
504 immunomodulatory response that improves cell retention and promotes both exosome production
505 and the secretion of independent cytokines. Given these mechanisms of action and the efficacy
506 of nMSCs in the immunocompetent rat MI model, nMSCs are a promising new cell type that is
507 uniquely positioned for successful translation to the clinic.

508

509 **STAR METHODS**

510 **Resource Availability**

511 The raw data, analytic methods, and study materials will be publicly available as online-only Data
512 Supplement. Study materials will be provided after a reasonable request. Inquiries can be directed
513 to the lead contact, Dr. Sunjay Kaushal. skaushal@luriechildrens.org.

514

515 **Materials availability statement**

516 This study did not generate new unique reagents.

517

518 **Data and code availability**

- 519 • No sequence data was generated
- 520 • No code data was generated
- 521 • Any additional information required to reanalyze the data reported in this paper is available
522 from the Lead contact on request.

523 **Experimental models and subject details**

524 **Human tissue samples for nMSCs preparation**

525 This study was approved by the Institutional Review Board and the Institutional Animal Care and
526 Use Committee at the University of Maryland School of Medicine. After parental or patient consent
527 was given, specimens from the right atrial appendage were obtained from neonatal ($n = 25$; $30 \pm$

528 20 mg) and adult patients (n = 43; 100 ± 30 mg) during routine cardiac surgeries. All adults were
529 undergoing coronary artery bypass grafting. From our cell bank, we randomly chose 7 neonatal
530 mesenchymal stromal cell lines from neonates having normal functioning myocardium (collected
531 during operations for structural abnormalities) and 7 adult mesenchymal stromal cell lines from
532 male patients with normal functioning myocardium for all experimental studies.

533

534 **Animal Studies**

535 This study was approved by Institutional Animal Care and Use Committee at the University of
536 Maryland School of Medicine. Both male and female rats were used for *in vivo* experiments.

537

538 **Generation of neonatal and adult mesenchymal stromal cells, cardiosphere-derived cells, 539 umbilical cord blood cells, and bone marrow–derived mesenchymal stem cells**

540 Cardiac neonatal and adult mesenchymal stromal cells were isolated from right atrial appendage
541 samples (Sharma et al., 2017). Human cardiosphere-derived cells were generated using a
542 modified version of the protocol (Mishra et al., 2011; Simpson et al., 2012). Human cord blood
543 mononuclear cells (Kaur et al., 2013) (Stem Cell Technologies #70007.1) and bone marrow–
544 derived mesenchymal stem cells (BM-MSCs) for *in vivo* experiments were cultured as described
545 previously (Hare et al., 2012). We randomly selected 3-7 different biological patient-derived stem
546 cell lines for all experimental studies.

547

548 **Flow Cytometry Analysis**

549 Heart tissue was harvested at day 5 post-MI from all the treated animals and was minced and
550 digested by Collagenase D (Roche) at 37°C for 50 minutes at rocking platform (180-200rpm).
551 After enzymatic digestion cells suspension was filtered through a 70-µm cell strainer (Fisher
552 Scientific #22363548) and centrifuged at 500g for 10 min, to lyse the red blood cells, cells pellet
553 was incubated in ACK lysing buffer (Gibco # A10492-01) at room temperature for 3-5 mins and

554 cells were washed with FACS washing buffer (2.5% FBS in PBS without calcium and
555 magnesium). Cells were re-suspended in washing buffer and samples were incubated with Fc-
556 Block (anti-rat CD16/CD32, 0.5 µg per 1 million cells) before incubation with isotype controls or
557 primary antibodies according to manufacturer's instructions. Cells were then washed with washing
558 buffer and approximately 2×10^5 events (cells) were analyzed by flow cytometry (LSR-Fortessa)
559 and populations gated as detailed below and sorted by FlowJo software. Supplementary Table 2
560 shows description of antibodies, including manufacture and antibody specificity.

561

562 **Gating strategy for flow cytometry analysis:**

563 T cells and T-regulator cells, cells were first gated (FSC-A vs. SSC-A) as lymphocytes. For Total
564 T cells, the lymphocyte gate is further analyzed for CD3 and CD8, For T-regulatory cells CD4
565 cells were gated and from this gate CD25⁺ and Fox-P3⁺ double positive cells were determined.
566 For macrophages, neutrophils, and dendritic cells, CD45 cells were gated. CD45 positive cells
567 were further analyzed for CD68 for macrophage, CD45⁺/CD11b⁺ /RP1⁺ (Neutrophils) and
568 CD11c⁺/MHC-11⁺ as dendritic cells.

569

570 **RNA Extraction and RT-PCR Analysis**

571 Total RNA was isolated from cells using miRNeasy kits from Qiagen and real-time PCR, according
572 to the manufacturer's instructions. A cDNA synthesis kit (Applied Biosystems, CA) was used to
573 reverse transcribe 500 ng RNA/reaction according to the manufacturer's protocol. We used 5 ng
574 cDNA for each sample in 20-µl PCR reactions. Each reaction was performed in triplicate using an
575 ABI Fast SYBR-Green reaction mix. Quantitect primer assays for each primer set were obtained
576 from Qiagen; probes were purchased from Thermofisher Inc. (Waltham, MA). Cycle threshold
577 (CT) values of the housekeeping gene were subtracted from the corresponding gene of interest.
578 The fold change of expression level for each gene was determined by the expression $2^{-\Delta\text{dCT}}$.

579 Final values were averaged, and results were represented as fold expression with the standard
580 error of the mean (SEM).

581

582 **μ Paraflo™ MicroRNA microarray Assay**

583 Microarray assays were performed using a service provider (LC Sciences, Inc). Four to 8 μ g of
584 total RNA samples were 3'-extended with a poly(A) tail using poly(A) polymerase. RNA was
585 amplified using a novel signal amplification strategy by labeling samples with an affinity tag for
586 signal amplification after hybridization. As the signal intensity increases from 1 to 65,535, the
587 corresponding color changes from blue to green, to yellow, and to red. An oligonucleotide tag
588 was then ligated to the poly(A) tail for later fluorescent dye staining. Hybridization was performed
589 overnight on a μ Paraflo microfluidic chip using a micro-circulation pump (Atactic Technologies)
590 (Gao et al., 2004). On the microfluidic chip, each detection probe consisted of a chemically
591 modified nucleotide coding segment complementary to a target microRNA (from miRBase,
592 <http://mirbase.org>) or other RNA (control or customer defined sequences) and a spacer segment
593 of polyethylene glycol to extend the coding segment away from the substrate. The detection
594 probes were made by *in situ* synthesis using PGR (photogenerated reagent) chemistry. The
595 hybridization melting temperatures were balanced by chemical modifications of the detection
596 probes. Hybridization used 100 μ L 6xSSPE buffer (0.90 M NaCl, 60 mM Na₂HPO₄, 6 mM EDTA,
597 pH 6.8) containing 25% formamide at 34°C. After RNA hybridization, a tag conjugated to Cy3
598 dye was circulated through the microfluidic chip for dye staining. Fluorescence images were
599 collected using a laser scanner (GenePix 4000B, Molecular Device) and digitized using Array-Pro
600 image analysis software (Media Cybernetics). Data were analyzed by first subtracting the
601 background and then normalizing the signals using a LOWESS filter (Locally weighted
602 Regression) using miRBase Release 20.0 (Bolstad et al., 2003). Signal p-values are provided
603 and a signal with p-value <0.01 is detectable.

604

605 **Single Cell Analysis**

606 Cardiac tissue was collected from three neonate and three adult patients and the respective
607 nMSCs and aMSCs were separated using magnetic bead sorting and sequenced using 10x
608 Chromium technology with Single Cell 3' v2 chemistry. The reads were aligned to the GRCh38
609 human reference genome using the Cell Ranger analysis pipeline (10x Genomics Cell Ranger
610 2.1.0) (Zheng et al., 2017). Raw counts were fed into the Scanpy single cell analysis library in
611 Python (Wolf et al., 2018). Doublets were filtered using the Scrublet method and the dataset was
612 filtered to remove cells with less than 1500 total transcripts or 780 distinctly expressed genes
613 (Wolock et al., 2019). The dataset was also filtered to remove cells with a greater than 20%
614 mitochondrial gene fraction. The dataset was further reduced to only include genes that were
615 expressed in at least 20 cells. Each batch was normalized using the SCRAN cell pooling
616 methodology and utilized a coarse Leiden clustering to identify initial cell pools (Lun et al., 2016).
617 Jurkat cells that were initially spiked into the samples for quality control purposes during
618 sequencing were filtered from the dataset using CD3E and CD3D gene expression to identify
619 cells with normalized expression greater than 1. The batch balanced k-nearest neighbors batch
620 correction algorithm was applied in conjunction with a ridge regression to align the individual
621 batches and remove sources of unwanted technical variance (Polański et al., 2020). The batch
622 corrected data was clustered using the Leiden algorithm at a resolution of 0.5. The differential
623 gene expression was computed on the clusters using non-batch corrected data using the
624 rank_genes_groups function in Scanpy with the default *t*-test method. The top 100 upregulated
625 genes were fed into the Metascape pathway analysis tool (Zhou et al., 2019). The final dataset
626 contained 61,979 cells, 60.5% of which were aMSCs and 39.5% were nMSCs.

627

628 **miRNA Selection**

629 Significantly differential expressed miRs (False detection rate (FDR<1.0%, P<0.05, fold change
630 more than 1.5)) between nMSC and aMSC were identified by miRNA microarray analysis. Our

631 screen identified miR34a-5p as highly and differentially expressed in aMSCs.

632

633 **Immunoblot Analysis**

634 Cells were lysed with radioimmunoprecipitation assay buffer (RIPA) (Cell Signaling Technology,
635 Boston, MA # 9806,) containing complete protease and phosphatase inhibitor cocktail (Roche
636 Applied Science, Indianapolis, IN #11836170001). Cell lysates were prepared, and protein
637 concentrations were determined using the bicinchoninic assay (BCA) method (ThermoFisher
638 Scientific, Waltham, MA #23209). SDS-PAGE (4–12% gels) (Invitrogen #NP0335BOX) were used
639 to resolve 40 µg of protein lysate. Proteins were transferred to PVDF membranes (Bio-rad
640 #1620177) using semidry or wet transfer methods and probed with specific antibodies to. We
641 analyzed 5 biological replicates for immunoblot analysis. The Odyssey system from Li-Cor
642 Biosciences was used for detection and quantitative analysis.

643

644 **AlamarBlue Cell Proliferation Assays**

645 Cell proliferation was assessed using alamarBlue (10% of the total volume of the medium), as per
646 the manufacturer's instructions. Briefly, 5,000 cells/well were seeded in 96-well plates in their
647 respective media. After overnight incubation at 37°C, 10 µl of alamarBlue Cell Viability Reagent
648 (Invitrogen cat #1933424, Carlsbad, CA) was added per well and absorbance was measured
649 immediately (basal absorbance) and after 3 h incubation at 37°C (proliferation absorbance). To
650 obtain the actual absorbance, the basal absorbance was subtracted from the proliferation
651 absorbance.

652

653 **Preparation of Conditioned Media and Paracrine Factor Quantification**

654 Following miR34a manipulation, aMSCs and nMSCs were grown in complete media until they
655 reached 85%–90% confluence ($\sim 1 \times 10^6$ cells). The cells were washed with warm Ham's F12
656 medium twice and changed to fresh Ham's F12 basal medium. Conditioning of the cells was

657 continued for 72 h to obtain secretome/total conditioned medium (TCM). Secretome was
658 precleared of cellular debris and particulate matter by centrifugation at 4,000 × g for 30 min,
659 followed by 10,000 × g for 30 min to remove microvesicles (Millipore Inc, Billerica, MA
660 #UFC900324). Total protein content was quantified using the BCA method. To normalize the
661 protein content we used the following formula: (concentration factor) × (total volume of
662 medium)/(total protein content of conditioned medium).⁸ The protein contents of the conditioned
663 media were quantified using the BCA method and normalized to a total of 1 mg protein. ELISA
664 was performed for human VEGFA, SDF-1, PDGFB, IGF-1, ANG-1, FGF2, SCF, and HGF in the
665 core facility at the University of Maryland School of Medicine using human-specific ELISA kits
666 (Millipore and R&D systems Inc. Billerica, MA), according to the manufacturer's protocol.

667

668 **Angiogenesis Assay**

669 The formation of tube-like structures was assessed in a Matrigel-coated 24-well plate (BD
670 Biosciences, San Jose, CA) (Sharma et al., 2017). Briefly, human umbilical vein cells (HUVEC-1,
671 ATCC PCS-100-010TM) were counted and seeded at a density of 20,000 cells/mm² on reduced
672 growth factor–containing Matrigel (BD Biosciences, San Jose, CA #354230,) with the addition of
673 endothelial manipulation in aMSCs and nMSCs or conditioned medium from Empty a control.
674 Cells were imaged after 6–12 h and a complete image of each well was reconstructed. The total
675 tube length was then measured using ImageJ64, NIH (<http://rsb.info.nih.gov/ij>).

676

677 **NanoSight Particle Analysis of Exosomes**

678 Exosomes from nMSCs and aMSCs after miR-34a overexpression and knockdown were isolated
679 and analyzed. Briefly, exosomes were purified from total conditioned medium (TCM) by size
680 exclusion chromatography using a Sepharose 2B column (Sigma-Aldrich #CL2B300) and eluted
681 fractions were analyzed using a NanoSight NS300 (405-nm laser diode) for the presence of
682 vesicles 40–120-nm in diameter.

683 Cell Transplantation and Echocardiography

684 MI was induced by permanent ligation of the left anterior descending (LAD) coronary artery in
685 immunodeficient (RNU rats, Charles River) / immunocompetent rats (Brown Norway, Charles
686 River) (weight: 160-220g). Briefly, heart was exposed via a left thoracotomy, and the proximal
687 LAD was ligated. One million cells were suspended in 100 µl vehicle (IMDM-base media without
688 any essential nutrients or growth factors) and injected into the myocardium at 4 sites adjacent to
689 the infarct while IMDM serves as placebo control. Baseline echocardiograms were acquired 1 day
690 after procedure (post-operative echocardiographic examinations at 24 h to insure similar extend
691 of induction of MI), 7 days and at 28 days post- MI. Two-dimensional and M-mode
692 echocardiography was performed using the VisualSonics Vevo 2100 ultrasound unit
693 (VisualSonics, Toronto, Canada) to assess metrics of left ventricular size and function. Images
694 were obtained from the parasternal long axis and the parasternal short axis at the midpapillary
695 level.

696 Myocardial Histology

697 Rat hearts were excised under anesthesia after collection of echocardiographic data and perfused
698 with 10% formalin solution, (Sigma Aldrich #HT501128). Tissues were cryopreserved using 30%
699 sucrose (prepared in 1xPBS) and embedded in OCT (Fisher Scientific, TissueTek #NC1029572).
700 Sections were cut to 7 µm using a commercial cryostat and stained for different antibodies
701 according to manufacturer's instruction. Cells and tissue sections were counterstained with 4',6-
702 diamidino-2-phenylindole (DAPI) nuclear stain (Sigma #F6057).

703

704 Myocardial Viability

705 The midline technique for infarct size determination was used (Sharma et al., 2017) . Briefly, the
706 infarct size was calculated using Masson's trichrome-stained sections at various levels along the
707 long axis. The stained sections were analyzed by ImagePro software. To calculate the viable and
708 nonviable tissue, the number of red pixels (viable tissue) and blue pixels (nonviable tissue) were

709 measured and the ratio of nonviable tissue/overall number of pixels was calculated. Six sections
710 per animal and at least 5-8 animals per group were analyzed.

711

712 **Lentivirus Production and Transduction**

713 Manipulation of gene expression was performed by lentiviral transduction. All lentiviruses were
714 produced in HEK293T. HEK293T cells (American Type Culture Collection, Manassas, VA) were
715 cultured in DMEM media (CellGro) supplemented with 10% fetal bovine serum (Thermofisher
716 Scientific #A38402-02). Lentivectors were co-transfected with the VSV-G envelope-expressing
717 plasmid pMD2.G (gift from Didier Trono, Addgene plasmid #12259) and packaging plasmid
718 psPAX2 (gift of Didier Trono, Addgene plasmid #12260) and concentrated using PEG-it (System
719 Biosciences). The titer of each lentivirus preparation was calculated based upon the amount of
720 virus required to yield 50% GFP⁺ cells following transduction of 100,000 MSCs. Cells were
721 transduced in 12-well dishes with increasing amounts of lentivirus in media supplemented with 8
722 µg/ml polybrene (Sigma Aldrich #TR-1003). Three days after transduction, the percentage of
723 GFP⁺ cells in each well were determined by flow cytometry using Accuri C6 (Becton Dickinson).
724 The amount of virus necessary to obtain 50% GFP⁺ cells was set to MOI = 0.5. Subsequent cell
725 transductions were performed at MOI = 2 (~90% GFP⁺ cells at day 3 days post-transduction) for
726 analysis of MSC phenotypes and function. In each experiment, transduction efficiency was
727 confirmed by flow cytometric determination of the percentage of GFP⁺ cell populations.

728

729 **Luciferase Assays**

730 All luciferase assays were conducted using the miRGlo vector (Promega #E1330), which co-
731 expresses firefly and Renilla luciferase. HEK293T cells (ATCCn CRL-3216) were transfected with
732 Lipofectamine 2000 (ThermoFisher Scientific #11668030). All experimental samples were
733 transfected with miR-Glo-based luciferase reporters and the miR34a versus miR550b miR mimic
734 (Dharmacon). Two days post-transfection, cells were harvested in passive lysis buffer and

735 luciferase values were quantified using a dual luciferase reporter assay kit (Promega #E1910)
736 according to the manufacturer's instructions on a Perkin Elmer Victor X3 Multilabel Reader. For
737 each condition, 3 independent wells were transfected per experimental replicate. Firefly luciferase
738 in each well was normalized to Renilla luciferase values from same well. The entire experiment
739 was repeated at least 3 times.

740

741 **Preparation of Dead nMSCs**

742 nMSCs (1 million cells/100 μ l) were frozen at -80°C and thawed at 55°C for 10 min. This freeze-
743 thaw cycle was repeated a total of 3 times to prepare dead MSCs. Cell debris was resuspended
744 in 100 μ l IMDM. Lipopolysaccharide (LPS, 10 $\mu\text{g}/100$ μ l, Sigma # L2630) was injected as a
745 positive control to induce an immune response following LAD ligation. The activation and the
746 increased CD68⁺ macrophage following LPS injection was measured in the explanted in infarcted
747 hearts by immunohistochemistry.

748

749 **Macrophage depletion**

750 To determine whether macrophages are important for nMSC-mediated MI recovery,
751 macrophages in rats were depleted using clodronate liposomes as described (Ito et al., 2017;
752 Vagnozzi et al., 2019; Wernli et al., 2009). Briefly, Brown-Norway rats were intraperitoneally
753 injected with clodronate liposomes (Encapsula Nano Sciences # CLD-8901) and Encapsome
754 (control liposomes prepared in PBS) were intraperitoneally (1 ml/100 g body weight) on pre-MI
755 and post MI days 1 and 5 on Brown Norway rats. One million nMSCs cells with and without
756 clodronate liposomes were injected. Macrophage depletion on day 5 was determined by
757 measuring CD68⁺ macrophages by immunohistochemistry in the explanted hearts.

758

759 **CD47 knockdown in nCPCs by siRNA**

760 Knockdown of CD47 protein expression in nMSCs was performed using CD47 siRNA
761 (ThermoFisher Scientific, Inc, #145977). Briefly, nMSCs were transfected with 100 nM siRNA at
762 60% confluency using Lipofectamine RNAiMAX (ThermoFisher Scientific, #13778030). The
763 transfected cells were incubated in a humidified incubator at 37°C and 5% CO₂. Following 72 h
764 of transfection, cells were harvested and CD47 knockdown efficiency was verified by immunoblot
765 analysis.

766

767 ***In Vitro* Phagocytosis Assays**

768 *In vitro* phagocytosis assays were performed using GFP⁺ MSCs prepared using the lentiviral
769 transduction system. Briefly, the monocyte cell line THP-1 (ATCC® # TIB-202) was differentiated
770 to M ϕ using 200 ng/ml phorbol 12-myristate 13-acetate (PMA, Sigma #P1585) and activated to
771 M ϕ 1 (inflammatory phenotype) using LPS (100 ng/ml) (LPS, Sigma #L2630). Red-stained M ϕ 1s
772 (PKH26, Red, Sigma #PKH26GL) and GFP-expressing aMSCs or nMSCs were co-cultured in
773 RPMI complete medium for 24 h in 8-well chamber plates. To determine if CD47 blockade induces
774 phagocytosis, nMSCs^{GFP+} were incubated with anti-CD47 (Bio X Cell #BE0283) or control isotype
775 antibodies (Bio X Cell #BP0297). The CD47 expression in nMSCs were blocked using anti-CD47
776 antibodies (Goto et al., 2014; Tseng et al., 2013; Zhang et al., 2016). Briefly, nMSCs (1 million
777 cells/100 μ l) were incubated with anti-CD47 (1 μ g/100 μ l) and isotype control antibody for 1 h at
778 4°C in HulaMixer Sample Mixer (ThermoFisher Scientific #15920D) Thereafter, cells were
779 centrifuged at 1000 rpm for 5 min and unbound residual CD47 antibody in the supernatant was
780 discarded. The antibody bound nMSC cell pellet was resuspended in 100 μ l of IMDM for *in vitro*
781 and *in vivo* phagocytosis. Similarly, to determine whether miR-34a overexpression inhibits CD47
782 expression and induces phagocytosis, nMSC were transduced with either the lentiviral vector
783 overexpressing miR-34a (GFP⁺) or the empty vector expressing lentivirus as a control. The CD47
784 inhibition by miR-34a over expression in nMSC was validated by immunoblot. Phagocytic cells

785 (yellow) and proliferating MSCs (green) were enumerated using an EVOS microscope. GFP⁺
786 MSCs, M ϕ , and phagocytic cells were enumerated using ImageJ. The experiment was repeated
787 at least 3 times to obtain consistent results.

788

789 ***In Vivo* Phagocytosis Assays**

790 *In vivo* phagocytosis assays were performed by transplanting 1 million aMSC^{GFP+}, nMSC^{GFP+}, anti-
791 CD47 nMSC^{GFP+}, isotype antibody nMSC^{GFP+}, miR34a^{GFP+} overexpressing nMSC, and vector
792 control^{GFP+} nMSC in rat MI model. Rats hearts collected after 48 h were sectioned and stained for
793 GFP⁺, CD68⁺ cells by immunohistochemistry using specific antibodies. Images were acquired
794 using an EVOS microscope and cell retention analyzed by GFP expression, inflammation by
795 CD68⁺ cells, and phagocytic cells were analyzed for GFP⁺ cells present within the CD68⁺ cells
796 (yellow color), respectively. Transplanted cell retention, CD68⁺ cells, and phagocytic cells were
797 enumerated using ImageJ. The experiment was repeated in at least 4 rats to observe consistent
798 results for comparative analysis.

799

800 **Pathway Enrichment and Upstream Regulator Analyses**

801 Ingenuity Pathway Analysis (IPA) software (Qiagen Inc, USA) was used to perform pathway
802 enrichment and upstream regulator analyses. A list of differentially expressed genes in a dataset
803 with a minimum of 1.5-fold change and $P < 0.05$ significance when compared between the 2
804 groups was loaded into IPA. To identify biological pathways that were significantly regulated ($P <$
805 0.05 ; > 0.05 ratio of differentially regulated genes involved in a pathway with the number of genes
806 associated with the pathway), core analysis was performed on uploaded datasets based on fold
807 change and P value significance in a dataset according to a standard protocol (Dyavar Shetty et
808 al., 2012). We performed upstream regulator analysis to identify secretory factors, signaling
809 mediators, and transcription factors that may not be differentially expressed at the transcriptional
810 level but are predicted to be altered or modified (e.g., phosphorylation, acetylation, methylation)

811 at the protein level, which may result in significant ($P < 0.05$ and $> \pm 2.0$ Z score) activation or
812 inhibition.

813

814 **Statistical Analysis**

815 Immunohistochemical analysis for GFP⁺, CD68⁺ and phagocytic cells *in vivo* were derived from
816 30 microscopic fields per tissue sample for each rat. Immunohistochemical data are
817 representative for 4-5 rats in each cohort. Data are presented as Box-Whiskers plot representing
818 median \pm SD. * $P < 0.05$, ** $P < 0.01$, *** $P < 0.001$, **** $P < 0.0001$, and 2-way ANOVA followed by
819 Bonferroni's multiple comparisons test (ejection fraction, fractional shortening), one-way ANOVA
820 followed by Tukey's multiple comparisons tests (fibrosis, immune cell analysis), Unpaired t test
821 (flow cytometric analysis). Prism software from Graphpad Inc was used for data analyses.
822 Comparative analysis of the cohorts was performed by t test followed by Mann Whitney test
823 (phagocytosis assay, miRNA expression) or more than 2 cohorts were compared by one way
824 ANOVA followed by Tukey's multiple comparisons test (paracrine analysis, angiogenesis,
825 exosomes analysis). A p value less than 0.05 indicated statistical significance.

826

827 **Acknowledgements**

828 We acknowledge Fern P finger for assistance in preparing this manuscript.

829

830 **Author Contributions** S.K., R.M. and M.G. conceived the study. R.M., M.G. S.S., L.D., W.C.,
831 L.C., P.S., X.F., A.J., J.H. A.S., G.B., M.A., D.M., A.T., and T.K. performed experiments and
832 generated all the data shown in the manuscript. S.K., P.Y., R.B., and C. C. provided theoretical
833 assessment of the project and advice in experimental design. S.K., R.M. S.S., D.L., M.E.D., R.B.,
834 J.M.H, and M.G. interpreted the data and wrote the manuscript.

835

836 **Statement of Declaration of Interest**

837 This work was supported by grants from the National Institute of Health to S.K. (HL141922,
838 HL139060, HL145644, HL118491-06A1). M.G. (2018-MSCRFF-4326 & 2020-MSCRFD-5338)
839 and R.M. (2018-MSCRFD-4329) were supported by the Maryland Stem Cell Research
840 Foundation. S.S. was supported by an American Heart Association Career Development Award
841 (18CDA34110282). J.R.H. was supported by F31HL154725 from the National Institutes of Health.
842 M.E.D. was supported by HL145644 from the National Institutes of Health. S.K. is the founder of
843 Neoprogen Inc. Joshua M. Hare reports having a patent for cardiac cell-based therapy and holds
844 equity in Vestion Inc. and maintains a professional relationship with Vestion Inc. as a consultant
845 and member of the Board of Directors and Scientific Advisory Board. Vestion Inc. did not play a
846 role in the design, conduct, or funding of the study. Dr. Joshua Hare is the Chief Scientific Officer,
847 a compensated consultant and board member for Longeveron Inc. and holds equity in
848 Longeveron. Dr. Hare is also the co-inventor of intellectual property licensed to Longeveron.
849 Longeveron did not play a role in the design, conduct, or funding of the study. The University of
850 Miami is an equity owner in Longeveron Inc., which has licensed intellectual property from the
851 University of Miami.

852

853

854

REFERENCES:

- Alvey, C., and Discher, D.E. (2017). Engineering macrophages to eat cancer: from "marker of self" CD47 and phagocytosis to differentiation. *J Leukoc Biol* 102, 31-40.
- Bolstad, B.M., Irizarry, R.A., Astrand, M., and Speed, T.P. (2003). A comparison of normalization methods for high density oligonucleotide array data based on variance and bias. *Bioinformatics* 19, 185-193.
- Chao, M.P., Weissman, I.L., and Majeti, R. (2012). The CD47-SIRPalpha pathway in cancer immune evasion and potential therapeutic implications. *Curr Opin Immunol* 24, 225-232.
- Dai, Y., Wang, S., Chang, S., Ren, D., Shali, S., Li, C., Yang, H., Huang, Z., and Ge, J. (2020). M2 macrophage-derived exosomes carry microRNA-148a to alleviate myocardial ischemia/reperfusion injury via inhibiting TXNIP and the TLR4/NF- κ B/NLRP3 inflammasome signaling pathway. *J Mol Cell Cardiol* 142, 65-79.
- Deuse, T., Hu, X., Gravina, A., Wang, D., Tediashvili, G., De, C., Thayer, W.O., Wahl, A., Garcia, J.V., Reichenspurner, H., *et al.* (2019). Hypoimmunogenic derivatives of induced pluripotent stem cells evade immune rejection in fully immunocompetent allogeneic recipients. *37*, 252-258.
- Duran, J.M., Makarewich, C.A., Sharp, T.E., Starosta, T., Zhu, F., Hoffman, N.E., Chiba, Y., Madesh, M., Berretta, R.M., Kubo, H., *et al.* (2013). Bone-derived stem cells repair the heart after myocardial infarction through transdifferentiation and paracrine signaling mechanisms. *Circ Res* 113, 539-552.
- Dyavar Shetty, R., Velu, V., Titanji, K., Bosinger, S.E., Freeman, G.J., Silvestri, G., and Amara, R.R. (2012). PD-1 blockade during chronic SIV infection reduces hyperimmune activation and microbial translocation in rhesus macaques. *J Clin Invest* 122, 1712-1716.
- Frangogiannis, N.G. (2012). Regulation of the inflammatory response in cardiac repair. *Circ Res* 110, 159-173.
- Galuppo, P., Vettorazzi, S., Hövelmann, J., Scholz, C.J., Tuckermann, J.P., Bauersachs, J., and Fraccarollo, D. (2017). The glucocorticoid receptor in monocyte-derived macrophages is critical for cardiac infarct repair and remodeling. *FASEB J* 31, 5122-5132.
- Gao, X., Gulari, E., and Zhou, X. (2004). In situ synthesis of oligonucleotide microarrays. *Biopolymers* 73, 579-596.
- Goto, H., Kojima, Y., Matsuda, K., Kariya, R., Taura, M., Kuwahara, K., Nagai, H., Katano, H., and Okada, S. (2014). Efficacy of anti-CD47 antibody-mediated phagocytosis with macrophages against primary effusion lymphoma. *Eur J Cancer* 50, 1836-1846.
- Hare, J.M., Fishman, J.E., Gerstenblith, G., DiFede Velazquez, D.L., Zambrano, J.P., Suncion, V.Y., Tracy, M., Ghersin, E., Johnston, P.V., Brinker, J.A., *et al.* (2012). Comparison of allogeneic vs autologous bone marrow-derived mesenchymal stem cells delivered by transendocardial injection in patients with ischemic cardiomyopathy: the POSEIDON randomized trial. *JAMA* 308, 2369-2379.
- Ito, T., Ishigami, M., Matsushita, Y., Hirata, M., Matsubara, K., Ishikawa, T., Hibi, H., Ueda, M., Hirooka, Y., Goto, H., *et al.* (2017). Secreted Ectodomain of SIGLEC-9 and MCP-1 Synergistically Improve Acute Liver Failure in Rats by Altering Macrophage Polarity. *Sci Rep* 7, 44043.
- Jaiswal, S., Jamieson, C.H., Pang, W.W., Park, C.Y., Chao, M.P., Majeti, R., Traver, D., van Rooijen, N., and Weissman, I.L. (2009). CD47 is upregulated on circulating hematopoietic stem cells and leukemia cells to avoid phagocytosis. *Cell* 138, 271-285.
- Kamerkar, S., LeBleu, V.S., Sugimoto, H., Yang, S., Ruivo, C.F., Melo, S.A., Lee, J.J., and Kalluri, R. (2017). Exosomes facilitate therapeutic targeting of oncogenic KRAS in pancreatic cancer. *Nature* 546, 498-503.
- Kaur, R., Sloan, L.A., Blanchard, A.D., Smith, J.L., Churcher, I., Wayne, G.J., and Ludbrook, S.B. (2013). A phenotypic screening approach in cord blood-derived mast cells to identify anti-

- inflammatory compounds. *J Biomol Screen* 18, 1223-1233.
- Konstandin, M.H., Toko, H., Gastelum, G.M., Quijada, P., De La Torre, A., Quintana, M., Collins, B., Din, S., Avitabile, D., Völkers, M., *et al.* (2013). Fibronectin is essential for reparative cardiac progenitor cell response after myocardial infarction. *Circ Res* 113, 115-125.
- Lim, J.Y., Park, M.J., Im, K.I., Kim, N., Jeon, E.J., Kim, E.J., Cho, M.L., and Cho, S.G. (2014). Combination cell therapy using mesenchymal stem cells and regulatory T-cells provides a synergistic immunomodulatory effect associated with reciprocal regulation of TH1/TH2 and th17/treg cells in a murine acute graft-versus-host disease model. *Cell Transplant* 23, 703-714.
- Lun, A.T., Bach, K., and Marioni, J.C. (2016). Pooling across cells to normalize single-cell RNA sequencing data with many zero counts. *Genome Biol* 17, 75.
- Majeti, R., Chao, M.P., Alizadeh, A.A., Pang, W.W., Jaiswal, S., Gibbs, K.D., Jr., van Rooijen, N., and Weissman, I.L. (2009). CD47 is an adverse prognostic factor and therapeutic antibody target on human acute myeloid leukemia stem cells. *Cell* 138, 286-299.
- Métayer, L.E., Vilalta, A., Burke, G.A.A., and Brown, G.C. (2017). Anti-CD47 antibodies induce phagocytosis of live, malignant B cells by macrophages. *Oncotarget* 8, 60892-60903.
- Mishra, R., Vijayan, K., Colletti, E.J., Harrington, D.A., Matthiesen, T.S., Simpson, D., Goh, S.K., Walker, B.L., Almeida-Porada, G., Wang, D., *et al.* (2011). Characterization and functionality of cardiac progenitor cells in congenital heart patients. *Circulation* 123, 364-373.
- Nahrendorf, M., Pittet, M.J., and Swirski, F.K. (2010). Monocytes: protagonists of infarct inflammation and repair after myocardial infarction. *Circulation* 121, 2437-2445.
- Polański, K., Young, M.D., Miao, Z., Meyer, K.B., Teichmann, S.A., and Park, J.E. (2020). BBKNN: fast batch alignment of single cell transcriptomes. *Bioinformatics* 36, 964-965.
- Rieckmann, M., Delgobo, M., Gaal, C., Büchner, L., Steinau, P., Reshef, D., Gil-Cruz, C., Horst, E.N.T., Kircher, M., Reiter, T., *et al.* (2019). Myocardial infarction triggers cardioprotective antigen-specific T helper cell responses. *J Clin Invest* 129, 4922-4936.
- Saha, P., Sharma, S., Korutla, L., Datla, S.R., Shoja-Taheri, F., Mishra, R., Bigham, G.E., Sarkar, M., Morales, D., Bittle, G., *et al.* (2019). Circulating exosomes derived from transplanted progenitor cells aid the functional recovery of ischemic myocardium. *Sci Transl Med* 11.
- Segers, V.F., and Lee, R.T. (2008). Stem-cell therapy for cardiac disease. *Nature* 451, 937-942.
- Seo, H.H., Lee, S.Y., Lee, C.Y., Kim, R., Kim, P., Oh, S., Lee, H., Lee, M.Y., Kim, J., Kim, L.K., *et al.* (2017). Exogenous miRNA-146a Enhances the Therapeutic Efficacy of Human Mesenchymal Stem Cells by Increasing Vascular Endothelial Growth Factor Secretion in the Ischemia/Reperfusion-Injured Heart. *J Vasc Res* 54, 100-108.
- Sharma, S., Mishra, R., Bigham, G.E., Wehman, B., Khan, M.M., Xu, H., Saha, P., Goo, Y.A., Datla, S.R., Chen, L., *et al.* (2017). A Deep Proteome Analysis Identifies the Complete Secretome as the Functional Unit of Human Cardiac Progenitor Cells. *Circ Res* 120, 816-834.
- Shiraishi, M., Shintani, Y., Ishida, H., Saba, R., Yamaguchi, A., Adachi, H., Yashiro, K., and Suzuki, K. (2016). Alternatively activated macrophages determine repair of the infarcted adult murine heart. *J Clin Invest* 126, 2151-2166.
- Simpson, D.L., Mishra, R., Sharma, S., Goh, S.K., Deshmukh, S., and Kaushal, S. (2012). A strong regenerative ability of cardiac stem cells derived from neonatal hearts. *Circulation* 126, S46-53.
- Telukuntla, K.S., Suncion, V.Y., Schulman, I.H., and Hare, J.M. (2013). The advancing field of cell-based therapy: insights and lessons from clinical trials. *Journal of the American Heart Association* 2, e000338.
- Tseng, D., Volkmer, J.P., Willingham, S.B., Contreras-Trujillo, H., Fathman, J.W., Fernhoff, N.B., Seita, J., Inlay, M.A., Weiskopf, K., Miyanishi, M., *et al.* (2013). Anti-CD47 antibody-mediated phagocytosis of cancer by macrophages primes an effective antitumor T-cell response. *Proc Natl Acad Sci U S A* 110, 11103-11108.
- Vagnozzi, R.J., Maillet, M., Sargent, M.A., Khalil, H., Johansen, A.K., Schwanekamp, J.A., York, A.J., Huang, V., Nahrendorf, M., Sadayappan, S., *et al.* (2019). An acute immune response

- underlies the benefit of cardiac stem-cell therapy. *Nature*.
- Vagnozzi, R.J., Maillet, M., Sargent, M.A., Khalil, H., Johansen, A.K.Z., Schwanekamp, J.A., York, A.J., Huang, V., Nahrendorf, M., Sadayappan, S., *et al.* (2020). An acute immune response underlies the benefit of cardiac stem cell therapy. *Nature* 577, 405-409.
- Vasandan, A.B., Jahnvi, S., Shashank, C., Prasad, P., Kumar, A., and Prasanna, S.J. (2016). Human Mesenchymal stem cells program macrophage plasticity by altering their metabolic status via a PGE. *Sci Rep* 6, 38308.
- Wehman, B., and Kaushal, S. (2015). The emergence of stem cell therapy for patients with congenital heart disease. *Circ Res* 116, 566-569.
- Wernli, G., Hasan, W., Bhattacharjee, A., van Rooijen, N., and Smith, P.G. (2009). Macrophage depletion suppresses sympathetic hyperinnervation following myocardial infarction. *Basic research in cardiology* 104, 681-693.
- Willingham, S.B., Volkmer, J.P., Gentles, A.J., Sahoo, D., Dalerba, P., Mitra, S.S., Wang, J., Contreras-Trujillo, H., Martin, R., Cohen, J.D., *et al.* (2012a). The CD47-signal regulatory protein alpha (SIRPa) interaction is a therapeutic target for human solid tumors. *Proc Natl Acad Sci U S A* 109, 6662-6667.
- Willingham, S.B., Volkmer, J.P., Gentles, A.J., Sahoo, D., Dalerba, P., Mitra, S.S., Wang, J., Contreras-Trujillo, H., Martin, R., Cohen, J.D., *et al.* (2012b). The CD47-signal regulatory protein alpha (SIRPa) interaction is a therapeutic target for human solid tumors. *Proc Natl Acad Sci U S A* 109, 6662-6667.
- Wolf, F.A., Angerer, P., and Theis, F.J. (2018). SCANPY: large-scale single-cell gene expression data analysis. *Genome Biol* 19, 15.
- Wolock, S.L., Lopez, R., and Klein, A.M. (2019). Scrublet: Computational Identification of Cell Doublets in Single-Cell Transcriptomic Data. *Cell Syst* 8, 281-291.e289.
- Xu, Q., Seeger, F.H., Castillo, J., Iekushi, K., Boon, R.A., Farcas, R., Manavski, Y., Li, Y.G., Assmus, B., Zeiher, A.M., *et al.* (2012). Micro-RNA-34a contributes to the impaired function of bone marrow-derived mononuclear cells from patients with cardiovascular disease. *Journal of the American College of Cardiology* 59, 2107-2117.
- Zhang, M., Hutter, G., Kahn, S.A., Azad, T.D., Gholamin, S., Xu, C.Y., Liu, J., Achrol, A.S., Richard, C., Sommerkamp, P., *et al.* (2016). Anti-CD47 Treatment Stimulates Phagocytosis of Glioblastoma by M1 and M2 Polarized Macrophages and Promotes M1 Polarized Macrophages In Vivo. *PLoS One* 11, e0153550.
- Zhang, S., Yeap, X.Y., DeBerge, M., Naresh, N.K., Wang, K., Jiang, Z., Wilcox, J.E., White, S.M., Morrow, J.P., Burrige, P.W., *et al.* (2017). Acute CD47 Blockade During Ischemic Myocardial Reperfusion Enhances Phagocytosis-Associated Cardiac Repair. *JACC Basic Transl Sci* 2, 386-397.
- Zhang, X., Chen, W., Fan, J., Wang, S., Xian, Z., Luan, J., Li, Y., Wang, Y., Nan, Y., Luo, M., *et al.* (2018). Disrupting CD47-SIRPalpha axis alone or combined with autophagy depletion for the therapy of glioblastoma. *Carcinogenesis* 39, 689-699.
- Zheng, G.X., Terry, J.M., Belgrader, P., Ryvkin, P., Bent, Z.W., Wilson, R., Ziraldo, S.B., Wheeler, T.D., McDermott, G.P., Zhu, J., *et al.* (2017). Massively parallel digital transcriptional profiling of single cells. *Nat Commun* 8, 14049.
- Zhou, Y., Zhou, B., Pache, L., Chang, M., Khodabakhshi, A.H., Tanaseichuk, O., Benner, C., and Chanda, S.K. (2019). Metascape provides a biologist-oriented resource for the analysis of systems-level datasets. *Nat Commun* 10, 1523.

Figure Legends

Figure 1. Cardiac functional outcomes following stem cell transplantation in the MI model.

Left ventricular ejection fraction (LVEF) **(a)** and fractional shortening (LVFS) **(b)** derived from echocardiography are shown for post-operative day (POD) 1 and POD 28 with different cell therapies (N = 6-9) in RNU rat MI model. At POD 1, no significant difference was observed. **(c)** At POD 28, Masson trichrome staining of hearts sections after nMSCs, or placebo control or stem cell types; quantitative assessment is shown in **(d)** (N = 5-8). LVEF **(e)** and LVFS **(f)** derived from echocardiography are shown for POD 1 and POD 28 for treatment with nMSCs compared with BM-MSCs, aMSCs, and placebo (N = 5-11) in immuno-component Brown-Norway rat MI model. Immunoblot analysis **(g-h)** and real time PCR analysis **(i)** showing the expression of HSF1 in BM-MSC, aCDCs, aMSC and nMSCs. Data were analyzed by One-way ANOVA using Prism Graphpad™ software and represented as mean ± SEM. (* $P < 0.05$, ** $P < 0.01$, *** $P < 0.001$ and **** $P < 0.0001$).

Figure 2. Immune cell analysis following MSC injection in the rat MI model.

Representative images of Day 2 heart tissues showing inflammatory CD68⁺CCR2⁺ **(a)** or CD68⁺CX3C1⁺ **(b)** macrophages and anti-inflammatory CD68⁺163⁺ macrophages **(c)** in the rat myocardium after injection of aMSCs, nMSCs, placebo, or sham controls (scale bars = 75 μm). Quantitative assessment of CD68⁺CCR2⁺ cells **(d)**, CD68⁺CX3C1⁺ cells **(e)**, and CD68⁺163⁺ cells **(f)** in MI hearts after nMSC injection, as compared with placebo controls (N = 4-5). Phenotypic characterization of macrophages (CD45⁺ CD68⁺), neutrophils (CD11b/c⁺/R1⁺), and regulatory T cells (Tregs; CD4⁺CD25⁺FoxP3⁺) in rat hearts following nMSC transplantation compared with placebo injection **(g)** (N = 5-6). Representative histograms show flow cytometry analyses of macrophages, neutrophils, and Tregs **(h)**. Data were analyzed by One-way ANOVA using Prism Graphpad™ software and represented as mean ± SEM. (* $P < 0.05$, ** $P < 0.01$, *** $P < 0.001$ and **** $P < 0.0001$).

Figure 3. Cardiac nMSCs evade phagocytosis. (a) Representative micrographs of human monocytes (THP-1) differentiated into macrophages (Mφs). (b) Immunoblot results show expression of the monocyte marker CD31 in monocytes and its reduction following Phorbol 12-myristate 13-acetate (PMA; differentiation) and LPS (activation) treatment. In contrast, the Mφ phenotypic marker CD68 and MHC-II were observed only with PMA and lipopolysaccharide (LPS) treatment. Glyceraldehyde 3-phosphate dehydrogenase (GAPDH) served as a loading control. (c) Representative images showing Mφ-mediated phagocytosis of nMSCs^{GFP+} or aMSCs^{GFP+} after 24 hours in co-culture. Scale bars = 75 μm. (d) Quantification of nMSCs^{GFP+} or aMSCs^{GFP+} (cell retention, green) phagocytosis by Mφs (PKH26, red) after 24 hours. (e) Representative images following injection of nMSCs^{GFP+} or aMSCs^{GFP+}. The nMSCs are more proliferative, have reduced CD68 expressing cells, and reduced phagocytosis compared with aMSCs. (scale bars = 75 μm). (f) Quantification of nMSC^{GFP+} retention and CD68⁺ phagocytic cells compared with aMSCs^{GFP+} following injection in MI rats (N = 4). Data were analyzed by Prism Graphpad™ software by non-parametric Mann Whitney test and represented as mean ± SEM. (**P*<0.05, ***P*<0.01, ****P*<0.001 and *****P*<0.0001).

Figure 4. RNA sequencing of nMSCs and aMSCs. (a) Graphical representations of mRNA sequencing data. The mRNAs are ranked in a volcano plot according to their statistical (*P* value) significance (-log *P*; y-axis) and the ratio of their relative abundance ratio (log₂-fold change; x-axis) in nMSCs (blue) and aMSCs (red). Histogram representation of genes with significantly increased mRNA (b) and their targets (c). (d) Uniform Manifold Approximation and Projection visualization of single-cell data collected from nMSCs (orange) and aMSCs (blue). (e) Results of Leiden clustering at a resolution of 0.5. (f) Heatmap of gene expression for selected genes within each cluster. (g) The percentage of cells from either adult or neonate patient age groups in each cluster. Neonate cells are especially overrepresented in Cluster 2, whereas adult cells are overrepresented in Cluster 3. (h) The top 20 up-regulated genes, as determined by Scanpy, for

Clusters 2 and 3. **(i)** Metascape heatmap of GO terms obtained from the top 100 up-regulated genes for Clusters 2 and 3. Up-regulated genes in Cluster 2 correlate with cell cycle and proliferative activity, whereas up-regulated genes in Cluster 3 correlate with increased leukocyte migration and cell death.

Figure 5. CD47 expression on nMSC inhibits phagocytosis. Immunoblots showing expression of CD47 in nMSCs and aMSCs (N = 3) **(a)** and quantification **(b)**. **(c)**. Comparative expression of miR-34a in BM-MSC, CDC, aMSCs and nMSCs **(d)** Representative images of *in vitro* phagocytosis assays of nMSCs^{α-CD47} and nMSCs^{α-isotype} (scale bars = 75 μm). **(e)** Quantification of nMSCs^{α-isotype} (cell retention, green), Mφs (PKH26, red) and phagocytic cells (yellow) compared to nMSCs^{α-CD47}. **(f)** Representative images of nMSC^{α-CD47} and nMSC^{α-isotype} phagocytosis assays in rat MI model. **(g)** Quantification of nMSCs^{α-isotype} (cell retention, green), CD68⁺ Mφ (red) and phagocytic cells (yellow) compared to nMSCs^{α-CD47} in the rat MI model (N = 4). The rat MI model transplanted with nMSCs^{α-CD47} showed reduced LVEF **(h)** and LVFS **(i)** compared with nMSCs^{α-isotype} (N = 5-11). **(j)** LVEF and LVFS **(k)** of rat hearts injected with nMSCs^{CD47siRNA} or nMSCs^{scr.siRNA} in the rat MI model (N = 5-11). Data were analyzed by Prism Graphpad™ software. Non-parametric Mann Whitney test (Fig. e and g) and One-way ANOVA (Fig. h-k) were used for comparative analysis. Data were represented as mean ± SEM. (**P*<0.05, ***P*<0.01, ****P*<0.001 and *****P*<0.0001).

Figure 6. miR34a-regulated paracrine secretion and exosomes in MSCs

(a) Volcano plot showing differential expression of miRNAs in nMSCs and aMSCs. **(b)** Principal Component Analysis (PCA) showing the distribution of different biological samples of nMSCs or aMSCs according to miRNA gene ontology of molecular function. **(c)** Histograms showing the expression of miR-664a, -664b, -34a, and -4485 in aMSCs compared with nMSCs. Quantitative expression of miR-34a in aMSC and nMSC **(d)**. Comparative expression of miR-34a in BM-MSC, CDC, aMSCs and nMSCs **(e)**, by RT-PCR (N = 6). Cell growth as measured by alamarBlue

assays in aMSCs^{34aKD} and nMSCs^{34aOE} (**f-g**). Quantification of p16 (**h**) and p21 (**i**) in aMSCs^{34aKD} by RT-PCR (N = 5). Quantification of p16 (**j**) and p21 (**k**) in nMSCs^{34aOE} by RT-PCR. (**l**) CD47 expression in nMSCs following miR34a overexpression. LVEF (**m**) and LVFS (**n**) of rat hearts injected with nMSCs^{34aOE} compared with nMSCs transduced with empty vector (nMSCs^{EV}), nMSCs, and IMDM (vehicle control) (N = 5-11). (**o**) Representative images of *in vitro* phagocytosis assays of nMSCs^{34aOE} and nMSCs^{EV} (scale bars = 75 μ m). nMSCs^{EV} (cell retention, green), M ϕ s (PKH26, red), and phagocytic cells (yellow) compared to nMSCs^{miR34a OE} were quantified using ImageJ (**p**). (**q**) Representative images of *in vivo* phagocytosis assays in the rat MI model showing phagocytosis, CD68⁺ cells, and retention of nMSCs^{34aOE} compared with nMSCs^{EV}. (**r**) Quantification of actively proliferating nMSCs ^{α -isotype} (cell retention, green), CD68⁺ M ϕ (red), and phagocytic cells (yellow) compared to nMSCs ^{α -CD47} in rat myocardium (N = 4). Data were analyzed by Prism Graphpad[™] software. One-way ANOVA (Fig. c – l, n and o) test and non-parametric Mann Whitney test (Fig. q and s) and were used for comparative analysis. Data were represented as mean \pm SEM. (* P <0.05, ** P <0.01, *** P <0.001 and **** P <0.0001).

Figure 7. Effect of miR-34a on the MSCs secretome:

Quantification of 7 cardioprotective paracrine factors from aMSC^{34aKD} (**a**) and nMSCs^{34aOE} (**b**) (N = 3-4). (**c**) Luciferase reporter plasmids were constructed with either the wild-type miR-34a 3'UTR segment containing the miR-34a binding site with PDGFB, HGF, IGF1, FGF2, and SCF. Luciferase activity was normalized by the ratio of the firefly and Renilla luciferase signals (N = 3). Tube formation assay in aMSCs^{34aKD} and nMSCs^{34aOE} (**d**) and quantification (**e-f**) (N = 4). (**g**) Representative images of neovessel (IB4) and arterioles (α -smooth muscle actin [α -SMA]) formation in rat myocardium transplantation of aMSCs^{34aKD} and nMSCs^{34aOE} and its quantification (**h**) (N = 4). Fibrosis at POD 28 after aMSC^{34aKD} (**m**) and nMSC^{34aOE} transplantation (**o**) and quantification (**n, p**) from MI rats (N = 6-8). Exosome concentration in total conditioned media (TCM) by NanoSight after gain and loss of miR-34a function in aMSCs (**q**) and nMSCs (**r**) (N = 4-

6). **(s)** NanoSight tracking analysis of exosome particle number and size distribution analyzed in TCM isolated from aMSCs^{34aKD} and nMSCs^{34aOE}. Immunoblot analysis of HSF1 and HSP70 expression levels in aMSCs and nMSCs **(t)**, HSP70 and HSF1 expression levels increased after aMSC^{34aKD} in aMSCs **(u)**, and miR-34^{OE} in nMSCs **(v)**. Exosome biogenesis genes VSP37A **(w)**, VSP25 **(x)**, and CHM7 **(y)** after HSF-1 overexpression (N = 4-6). Data were analyzed by Prism Graphpad[™] software. One-way ANOVA was used for comparative analysis. Data were represented as mean ± SEM. (* $P < 0.05$, ** $P < 0.01$, *** $P < 0.001$ and **** $P < 0.0001$).

Video 1. Exosome nanoparticles observed in clarified TCM from aMSCs by NanoSight tracking analysis.

Video 2. Exosome nanoparticles observed in clarified TCM from aMSCs^{34aKD} by NanoSight tracking analysis.

Video 3. Exosome nanoparticles observed in clarified TCM from nMSCs^{34aOE} by NanoSight tracking analysis.

Video 4. Exosome nanoparticles observed in clarified TCM from nMSCs by NanoSight tracking analysis.

Supplemental Data 1 – MultiArray analysis data for miRNA

Supplemental Data 2 - RNAseq analysis

Fig.1

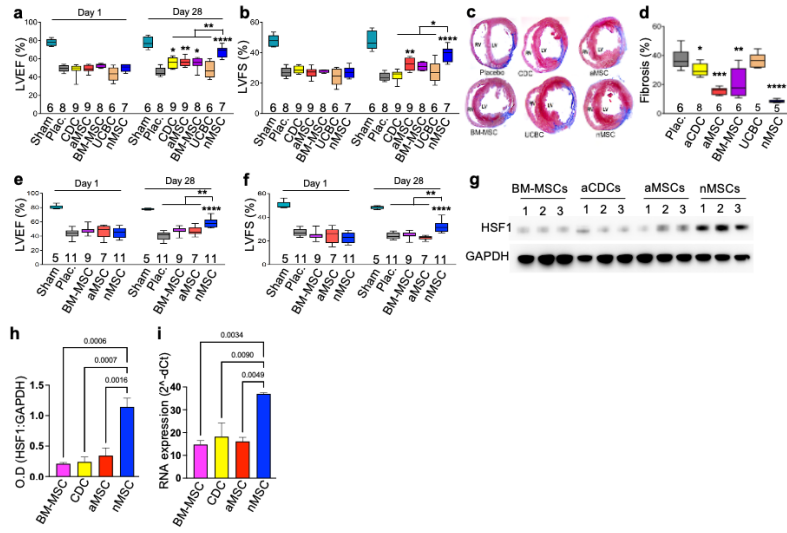


Fig.2

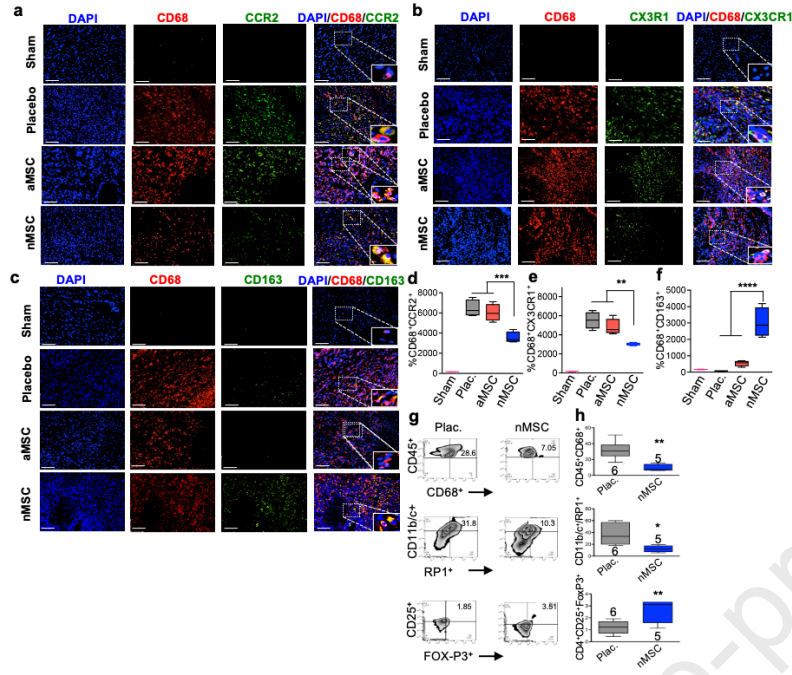


Fig.3

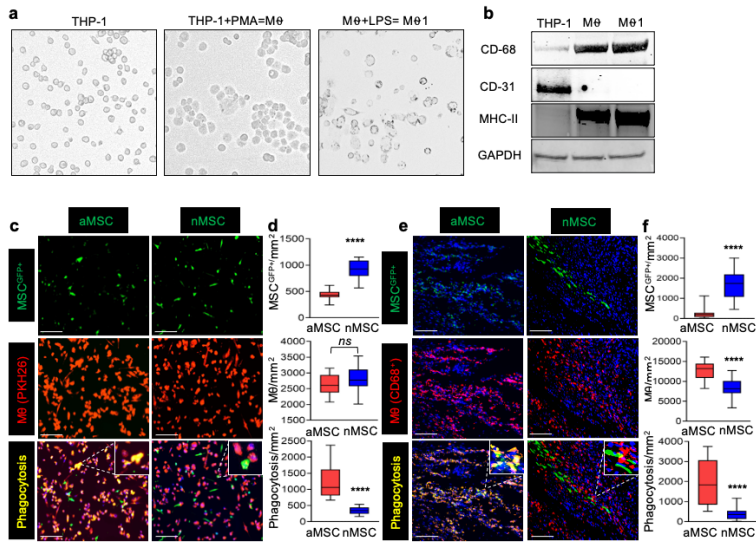


Fig.5

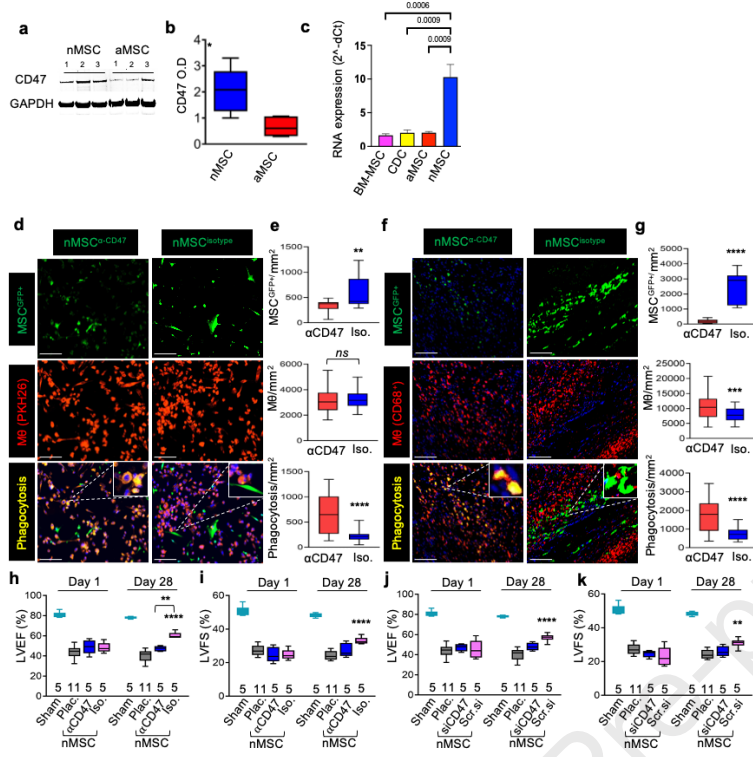


Fig.6

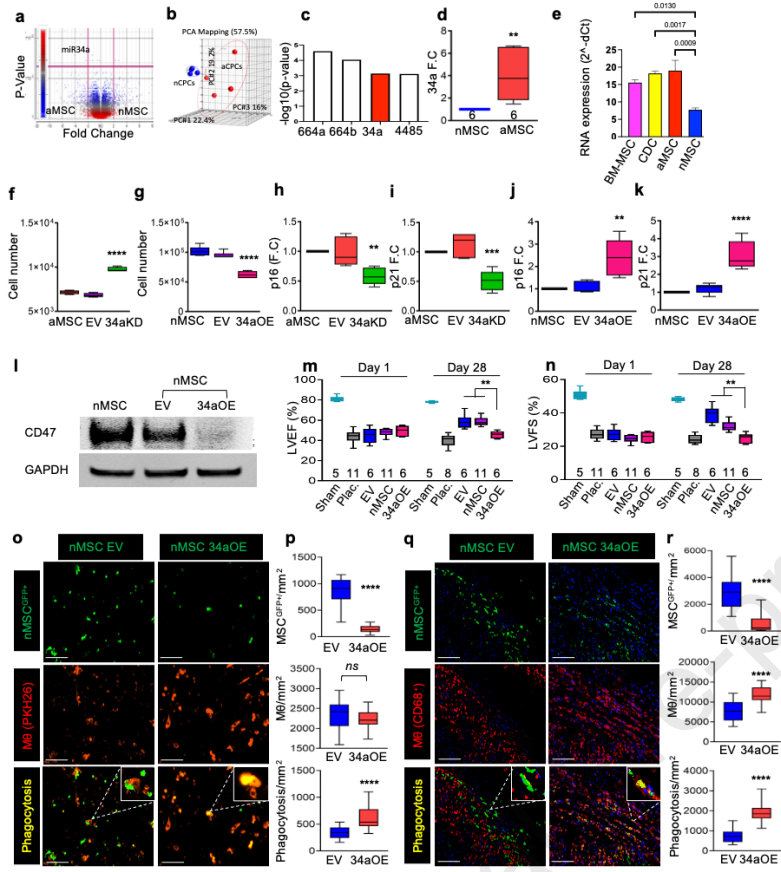
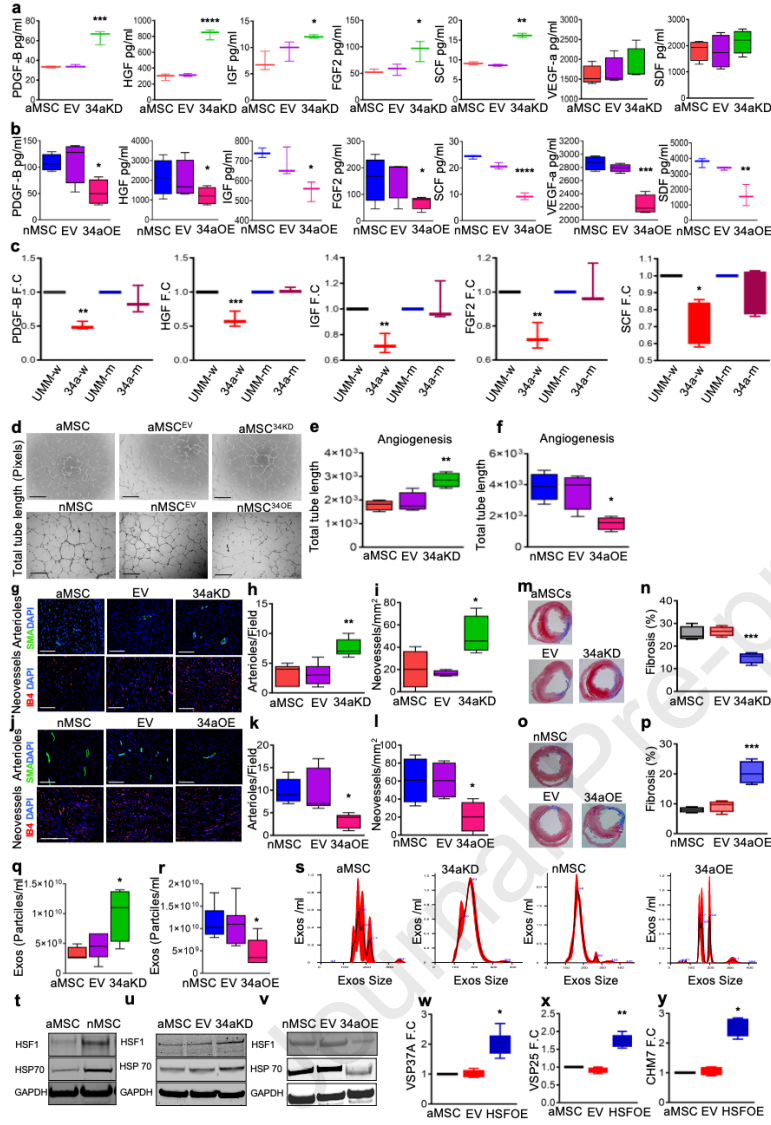


Fig.7



Highlights

- nMSCs are the most potent cell type yet to recover injured myocardium
- CD47 assisted immune evasion increases nMSCs' retention
- miR34a-5p regulate CD47 and the composition of nMSCs secretome

Journal Pre-proof

Table 1. Key resources table

Antigen	Catalogue No.	Source	Fluorochrome
Antibody for Flow Cytometry			
C-kit	561443	BD	APC
CD90	559869	BD	APC
CD105	561443	BD	PE
CD45	561443	BD	PE
CD34	sc-7045	SCBT	Goat pAb
CD31	561443	BD	FITC
CD3	557030	BD	APC
CD4	561578	BD	PE-Cy7
CD8	561614	BD	V450
CD25	17-0390-82	eBioscience	APC
FoxP3	320008	Biolegend	PE
CD45	202205	Biolegend	FITC
CD68	MCA341A488	BioRad	FITC
CD163	NBP2-39099	Novus	AF647
CD11c	11-0114-82	Invitrogen	FITC
CD11b/c	562222	BD	PE-Cy7
MHCII	17-0920-82	BD	APC
RP1	550002	BD	PE
CD16/CD32	553142	BD	Fc Block
Antibody for IHC			
IB4	121413	Invitrogen	AF 594
SMA	F3777	Sigma	FITC
CD68	ab31630	Abcam	Mouse pAb
CD163	ab199427	Abcam	Rabbit pAb
CCR2	ab273050	Abcam	Rabbit pAb
CX3R1	ab8021	Abcam	Rabbit pAb
Antibody for <i>in vitro</i> and <i>in vivo</i> phagocytosis			
CD47	BE0283	Bio X Cell	Mouse mAb
Isotype Control	BP0297	Bio X Cell	IgG1 Ab
GFP	MAB3580	Millipore	Mouse mAb
Antibody for Immunoblot			
CD47	ab108415	Abcam	Rabbit mAb
HSF1	4356s	CST	Rabbit mAb
HSP70	610607	BD	Mouse mAb
GAPDH	MAB374	Millipore	Mouse mAb
CD68	ab31630	Abcam	Mouse pAb

CD31	ab24590	Abcam	Mouse pAb
MHC-II	ab55152	Abcam	Mouse pAb
LAMP-2	ab203224	Abcam	Rabbit pAb
TSG101	612697	BD	Mouse mAb
RAB27A	ab108983	Abcam	Rabbit mAb
Reagents			
DAPI	F6057	Sigma	
Calcein, AM	C1430	Thermofisher Sci.	